AD-A043 259 NAVAL RESEARCH LAB WASHINGTON D C F/G 4/1
NUMERICAL MODELING OF AURORA VOLUME I OF THE CALENDAR YEAR 1975--ETC(U)
APR 77

UNCLASSIFIED NRL-MR-3462 NL

1 OF 2
AD
A043 259

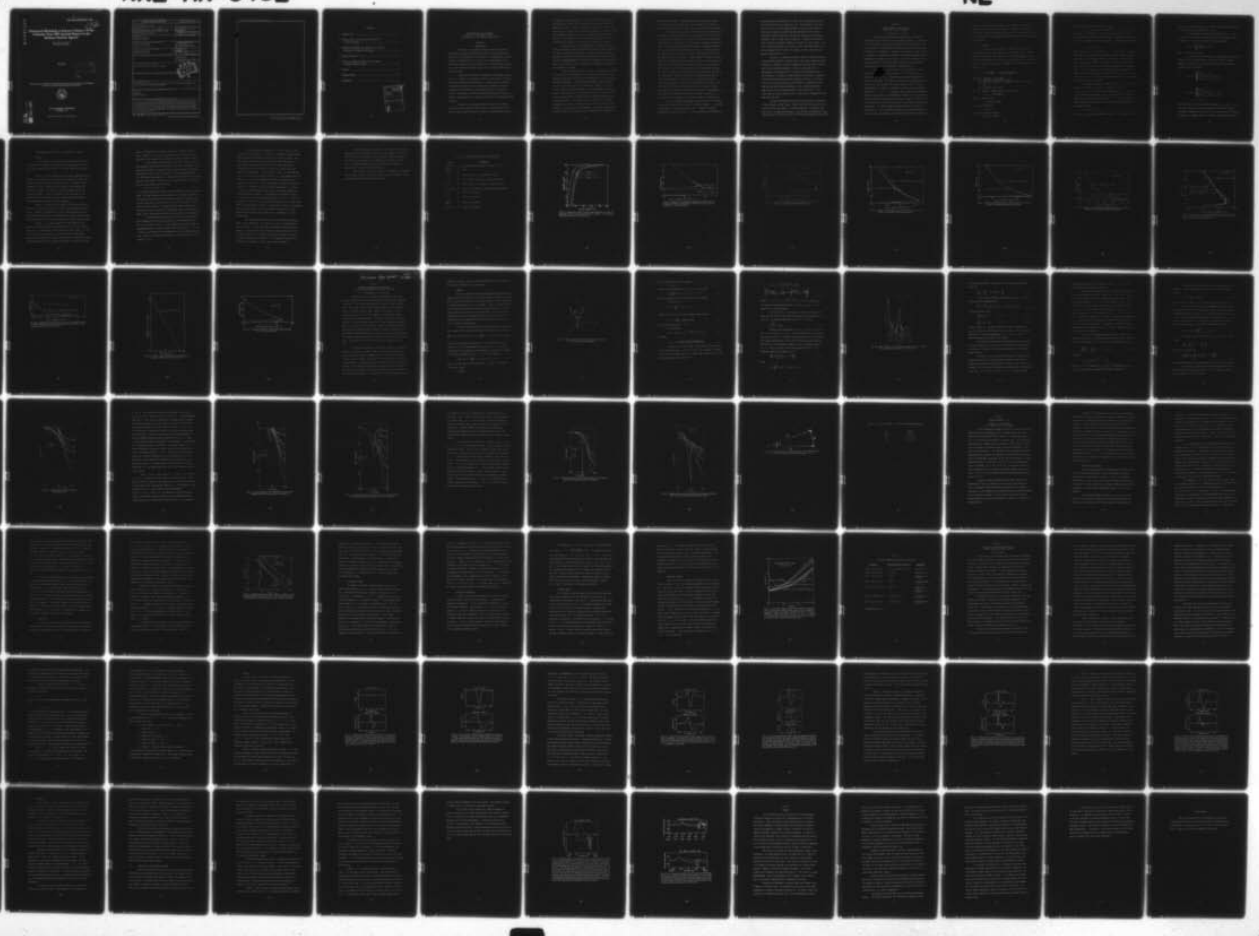

NRL Memorandum Report 3462

12

Numerical Modeling of Aurora Volume I of the Calendar Year 1975 Annual Report to the Defense Nuclear Agency

Plasma Dynamics Branch
Plasma Physics Division

April 1977

This research was sponsored by the Defense Nuclear Agency under subtask L25-AAXHX633, work unit 15, work unit title Numerical Auroral Models.

NAVAL RESEARCH LABORATORY
Washington, D.C.

SECURITY CLASSIFICATION OF THIS PAGE (When Data Entered)

REPORT DOCUMENTATION PAGE		READ INSTRUCTIONS BEFORE COMPLETING FORM
1. REPORT NUMBER NRL Memorandum Report 3462	2. GOVT ACCESSION NO.	3. RECIPIENT'S CATALOG NUMBER
4. TITLE (and Subtitle) NUMERICAL MODELING OF AURORA VOLUME I OF THE CALENDAR YEAR 1975 ANNUAL REPORT TO THE DEFENSE NUCLEAR AGENCY		5. TYPE OF REPORT & PERIOD COVERED Interim report on a continuing NRL problem. 6. PERFORMING ORG. REPORT NUMBER
7. AUTHOR(s) Plasma Dynamics Branch Plasma Physics Division		8. CONTRACT OR GRANT NUMBER(s)
9. PERFORMING ORGANIZATION NAME AND ADDRESS Naval Research Laboratory Washington, D.C. 20375		10. PROGRAM ELEMENT, PROJECT, TASK AREA & WORK UNIT NUMBERS NRL Problem H02-35 DNA Subtask L25-AAXHX633
11. CONTROLLING OFFICE NAME AND ADDRESS Defense Nuclear Agency Washington, D.C. 20305		12. REPORT DATE April 1977 13. NUMBER OF PAGES 121
14. MONITORING AGENCY NAME & ADDRESS(if different from Controlling Office)		15. SECURITY CLASS. (of this report) UNCLASSIFIED 15a. DECLASSIFICATION/DOWNGRADING SCHEDULE

16. DISTRIBUTION STATEMENT (of this Report)

Approved for public release; distribution unlimited.

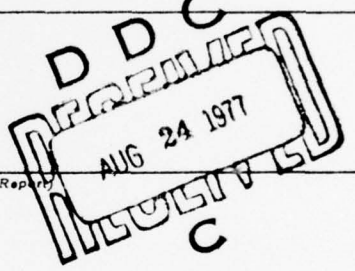

17. DISTRIBUTION STATEMENT (of the abstract entered in Block 20, if different from Report)

18. SUPPLEMENTARY NOTES

This research was sponsored by the Defense Nuclear Agency under subtask L25-AAXHX633, work unit 15, work unit title Numerical Auroral Models.

19. KEY WORDS (Continue on reverse side if necessary and identify by block number)

Aurora
Ionosphere
Particle precipitation

20. ABSTRACT (Continue on reverse side if necessary and identify by block number)

Work on aurora models by the Plasma Dynamics Branch of NRL for the year 1975 is reported. Correlations between auroral phenomena and high altitude nuclear explosion effects are discussed. An improved proton deposition code is described which includes cross sections for O_2, O and N_2 interactions with protons. The accuracy of the NRL electron deposition code for large angle scattering has been confirmed by a study of electron backscatter. An analysis of NO densities observed in auroral arcs is also presented. The report concludes with a presentation of recent improvements in the NRL auroral electrodynamic models.

DD FORM 1 JAN 73 1473 EDITION OF 1 NOV 65 IS OBSOLETE
S/N 0102-014-6601

SECURITY CLASSIFICATION OF THIS PAGE (When Data Entered)

CONTENTS

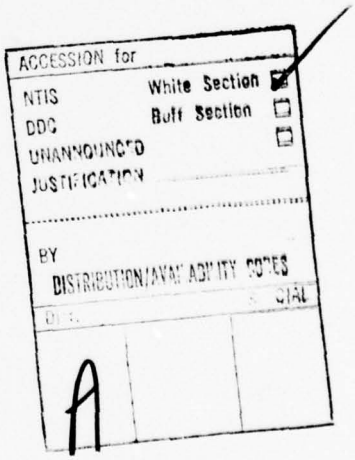

NUMERICAL MODELING OF AURORA
Volume I of the Calendar Year 1975
Annual Report to the Defense Nuclear Agency

Section 1

INTRODUCTION

At the core of the modern defensive systems are lines of communication serving as intelligence links for the initiation and direction of countermeasures. Confidence in a communication system's immunity to disruption is a function of one's understanding of the large scale changes that can be induced in the communications environment by both natural and other means, such as a high altitude nuclear explosion (HANE).

A HANE causes ionospheric disturbances from prompt gamma-ray, x-ray, UV, optical, or IR emissions, from late time motion of ionized debris and emissions from that debris. A complex series of physical and chemical reactions can be initiated with consequent enhanced ionization and perturbation of the ambient electric and magnetic fields. The program of the NRL Plasma Dynamics Branch is designed to produce reliable models for predicting ionospheric disturbances produced by HANEs.

Confidence in a numerical model derives from the model's ability to produce results consistent with a suitably complete and accurate observational data base. However, the observational data for

the response of the ionosphere to nuclear events is insufficient and the augmentation of the data is precluded by treaty restrictions on atmospheric testing. Under these circumstances, what is needed is a natural source of large scale ionospheric disturbances for which sufficient observations have been made. In addition there must be some parallels in the physics of the natural event and that of a HANE. The disturbances responsible for the aurora meet these requirements.

HANEs and auroras are characterized by energetic charged particles streaming along geomagnetic field lines and interacting with the ambient atmospheric constituents. Particle energies, degrees of ionization and heating rates differ between the two events, but ample theoretical correlations exist to make one's capability for modeling the aurora a good measure of one's capability for modeling the response of the ionosphere to a HANE.

Auroral models also help to provide a link between the modeling of the late time development of scintillation sources from HANE induced disturbances and scintillation observations (e.g. the Wideband Satellite Experiment). HANE phenomenology models provide as output the basic or initial state of the ionospheric plasma (i.e. electric fields, currents and plasma densities) in the immediate aftermath of a nuclear event and this in turn serves as the input for programs which follow the development of irregularities in those regions where the plasma is unstable. The auroral models are analogous to the HANE phenomenology models in that their output is the basic state of the ionosphere, but for an auroral disturbance. The auroral precipitation patterns which serve as input for auroral models can be supplied by

satellite observations. The plasma densities, currents and electric fields which the model computes are also observable by satellite and ground based radar and thus a check on the auroral model is available.

An auroral model in which confidence has been established can, in conjunction with observations on the ionospheric basic state, serve as a check on the programs used to model both HANE and aurora-induced irregularities. Observation of the ionospheric parameters necessary as input for the programs which model the formation of irregular regions are, for practical reasons, limited in coverage. Much scintillation data will be taken in regions for which no observations of the basic ionospheric state have been made. Auroral models, in which the output quantities are computed self-consistently, can be used to determine the missing data points, thereby extending the scope of the scintillation observations. A more important consequence of this derives from the fact that the model can provide the basic state parameters over much of the auroral oval. Smaller scale computer programs then are used to follow the development of irregularities in regions where plasma instabilities prevail. These are the same codes that are used in the HANE program. The output of these codes serves as input to signal propagation codes which predict scintillation effects. Comparisons of the computed and observed scintillations provides a measure of the reliability of the programs used to model ionospheric irregularities.

NRL has continued to progress along three lines of investigation which form the core of the auroral modeling programs: (1) particle interactions, (2) chemical reactions, and (3) changes in ambient ionospheric currents and fields. The proton deposition code PRODEP has

been improved by the addition of O_2 and O to the original code which had provided only for the presence of N_2. The influence of the geomagnetic field in proton energy degradation has also been included. Other work on particle interactions has included a study of backscattered electrons which has confirmed the accuracy of the electron deposition code for large angle scattering. A summary of the year's work on particle interaction appears in section 2 of this volume. The work on particle deposition in sections 2 and 3 was done early in CY 75 and was stopped in FY 76 under the guidance of DNA. Note that this annual report covers CY 75.

Section 4, on auroral chemistry, contains a critical analysis of NO densities observed in auroral arcs. This study demonstrates the importance of having an accurate knowledge of even the minor constituents in the disturbed atmosphere. Finally we conclude with a presentation of improvements in the auroral electrodynamic models. The importance of anomalous plasma processes on structure of electric fields and current systems has been studied in detail, as the structure of the fields and currents are important to ionospheric plasma stability and scintillation phenomena. Also, we present improved model results for the midnight region of the auroral oval. It is these types of results which will be of great use in interpreting Wideband Satellite Data.

The work performed at NRL during the past year is summarized in the remainder of this volume. Much of this work has been previously reported in NRL Memo Reports, at several symposia, in technical journals, and at DNA sponsored meetings. The principal contributors in each technical area are listed as authors of the section describing that work.

Section 2

IMPROVED MODEL TO STUDY PROTON DEPOSITION IN THE ATMOSPHERE

J. E. Rogerson and J. Davis

The deposition of energetic particles into the earth's atmosphere causes an abundance of interesting phenomena. In addition to the spectacular visual display produced by auroral emissions, the auroras provide a unique means for studying the complex of mechanisms occurring in the atmosphere. Knowledge of the causes of these effects is important in assessing the influence the disturbed atmosphere has on communication systems and their design. Also, since enhanced ionization is generated in the polar region, changes in the atmosphere's characteristics can be investigated during PCA events.

Many studies of the auroral electron deposition[1-8] and proton deposition[9-14] has been reported. In an earlier report, a simplified model based on a continuous-slowing-down approximation (CSDA) was described. This model contained only one atmospheric constituent, N_2, and neglected the earth's magnetic field. In this revised model, the number of atmospheric constituents is extended by including N_2, O_2, and O. By assuming a dipole model of the geomagnetic field, an expression for the differential element of arc length traversed by a charged particle spiraling around a magnetic field line[16-17] is incorporated into the CSDA to produce a more realistic proton energy degradation. The charge exchange formalism as given by Allison[18] is generalized to a three component atmosphere and a charge-equilibrated flux of protons and hydrogen atoms is generated from which atmospheric

excitation and ionization processes can be calculated. Secondary electron effects are treated as before[15]. Finally, total ionization results are presented and compared with results of the previous model[15] and with similar calculations by Eather and Burrows[9], who used a different technique.

2.1 THE MODEL

A charged particle moving in a magnetic field follows a spiral path about the field lines due to the Lorentz force. The arc length of this spiral path depends on the particle's charge, velocity, mass, and pitch angle with respect to the given field line. An equation for the differential element of arc length of the spiral path can be given as [16,17]

$$ds = \left\{ \frac{(1-3x/4)}{(1-x)} \cdot \frac{x^3}{x^3-\sin^2\alpha_e \sqrt{4-3x}} \right\}^{\frac{1}{2}} dr \ , \qquad (2.1)$$

where ds = increment of arc length,
dr = increment of geocentric distance,
r_e = equatorial radius of the magnetic field line (L shell),
$x = r/r_e$,
α_e = equatorial pitch angle.

Eq. (2.1) assumes a dipole magnetic field given by

$$B(r,\lambda) = M\sqrt{1+3\sin^2\lambda} \ / \ r^3 \ , \qquad (2.2)$$

where M = dipole moment

λ = magnetic latitude.

λ and r are related by

$$r = r_e \cos^2\lambda \ . \qquad (2.3)$$

The first adiabatic invariant

$$\sin^2\alpha/B = \text{constant} \qquad (2.4)$$

is also included, where α is the pitch angle.

Eq. (2.1) contains a singularity at x = 1, or r = r_e. This singularity corresponds to a point in the equatorial plane. For auroral studies, high latitude regions are of primary interest, and it is therefore reasonable to avoid this point. A singularity also occurs for

$$x^3 - \sin^2 \alpha_e \sqrt{4-3x} = 0,$$

which corresponds to a mirror point ($\alpha = \pi/2$). This second singularity corresponds to an initially downward-moving particle being reflected upward due to the converging magnetic field lines. Such a particle does not penetrate as deeply as it might if it had a smaller pitch angle; hence, it does not produce as much ionization as it otherwise might. Also, the treatment of "mirroring" particles introduces further complexities into the calculation. For this reason, and because the aim is to study the maximum perturbations created in the atmosphere, this singularity is also avoided.

By assuming a spherical earth of radius a, Eq. (2.1) can be taken as a function of altitude z by setting r = a+z; then x = (a+z) / r_e. For a given altitude difference, $z_1 - z_2$, Eq. (2.1) can be numerically integrated from z_1 to z_2 to give the arc length traveled by the particle in going from z_1 to z_2. Then, by using the CSDA as described in Reference 15, the proton energy degradation is computed as follows:

$$\Delta E = N_t (z_1) L_p (E,z_1) \Delta S , \qquad (2.5)$$

where $N_t(z_1)$ is the total atmospheric density at z_1, $L_p(E,z_1)$ is the

total proton loss function at z_1 for energy E, and ΔE, and ΔS is the arc length traversed in going from z_1 to z_2.

The individual loss function for protons in N_2, O_2, and O are adapted from analytic expressions given by Green and Peterson[19]. At altitude z, the total loss function is computed from

$$L_p(E,z) = \sum_{i=1}^{3} \frac{N_i(z)}{N_t(z)} L_{pi}(E,z), \tag{2.6}$$

where i is the species index.

At a given altitude and energy, a generalized charge equilibrated flux is calculated based on Allison's[18] charge exchange formalism. The generalized equilibrated fraction of protons and hydrogen atoms are given by

$$F_1(E,z) = \frac{\sum_i N^i(z)\, \sigma_{01}{}^i(E)}{\sum_i N^i(z)\, [\sigma_{01}{}^i(E) + \sigma_{10}{}^i(E)]}, \tag{2.7}$$

$$F_o(E,z) = \frac{\sum_i N^i(z)\, \sigma_{10}{}^i(E)}{\sum_i N^i(z)\, [\sigma_{01}{}^i(E) + \sigma_{10}{}^i(E)]}$$

$$= 1 - F_1(E,z),$$

where the index i runs over the three species N_2, O_2, and O. σ_{10} is the cross section for charge exchange of a proton with a neutral (creating a hydrogen atom), and σ_{01} is the cross section for electron stripping of a hydrogen atom by a neutral (creating a proton again).

For a given process α involving proton impact on species i, a volume production rate at altitude z for a given proton flux ϕ (E) is

$$P^{i}_{p\alpha}(z) = N^{i}(z) \int F_1(E,z)\, \sigma^{i}_{p\alpha}(E)\, \phi(E)\, dE, \tag{2.8}$$

and similarly for hydrogen atom impact processes with $F_1(E,z)$ replaced by $F_o(E,z)$.

To describe the creation of secondary electrons of kinetic energy T by direct ionization processes, an energy-differential cross section of the form

$$S(E,T) = d\sigma(E)/dT$$

$$= \frac{\sigma_{ion}(E)}{\Gamma \tan^{-1}\left(\frac{T_{max}}{\Gamma}\right)} \left[1 + T^2/\Gamma^2\right]^{-1} \tag{2.9}$$

as given by Edgar, Miles, and Green[14] is used. For E in keV, and T_{max} in eV,

$$T_{max} = 2.18\ E. \tag{2.10}$$

This is equivalent to a form given by Banks, Chappell, and Nagy[3] for secondary electron production from electron impact ionization. By using the Γ values given in Reference 3 and the value of 22 eV given by Reference 14 for proton impact ionization of N_2, Γ values for proton impact ionization of O_2 and O can be obtained by scaling. The same S(E,T) was used for both proton and hydrogen atom impact on the same target gas because of insufficient data. Secondary electrons created by the charge exchange cycle are treated exactly as in Reference 14; i.e.,

$$S_{01}(E,T) = \sigma_{cycle}(E)\, \alpha e^{-\alpha T} (1-e^{-\alpha T_{max}})^{-1}, \qquad (2.11)$$

where σ cycle - $\sigma_{10}\,\sigma_{01}/(\sigma_{10} + \sigma_{01})$, and $1/\alpha$ is taken to be 5 eV for each species. Excitation and ionization by secondary and higher order electrons are treated by the method described by Dalgarno[7] and used by Julienne[8].

2.2 CROSS SECTIONS

The principal sources for H and H^+ impact cross section data are the review articles by McNeal and Birely[20,21]. The charge exchange cross section for O_2 is taken from Stebbings, et al.[22] for lower energies and by doubling the O charge exchange cross section as given by Allison[18] for the higher energies. The electron stripping reaction of H by O_2 is obtained from doubling the O cross-section data given by Allison[18] for the same process. The charge exchange cross section for O was taken from Neynaber, et al.[23] for energies below one kev and from McNeal and Birely[21] for higher energies. Many of these cross sections do not extend below two to four keV in energy and were extrapolated to lower energies.

The input cross-section data points for proton, hydrogen atom, and electron impact processes are fitted to the points on a chosen energy grid E by a cubic spline representation as a function of ln E. In this way, only a few experimental points are needed for a good representation, and analytic fits to cross sections are not required. The cross sections are extrapolated to high energies by using the appropriate asymptotic forms.

The electron cross sections are summarized in Table 2.1

2.3 RESULTS

In this section, some results of the revised proton deposition model are presented and compared with the previous model[15] and with similar calculations by Eather and Burrows (hereafter denoted by EB).

Figure 2.1 shows a comparison of the energy degradation of an incident 100 kev proton in the two NRL proton deposition models for a pure N_2 atmosphere; in these calculations, the 1965 Jacchia[24] model atmosphere is used. Results for pitch angles of zero degrees and for about 45 degrees are shown when the earth's magnetic field is taken into account. It can be clearly seen that the effect of the magnetic field is to greatly increase energy degradation and thus reduce the penetration depth into the atmosphere.

Figure 2.2 shows the total number of N_2^+ ions produced as a function of altitude for these same 100 keV proton deposition calculations. At higher altitudes there is very little difference, but at lower altitudes, fewer ions are created when the earth's magnetic field is included because of the reduced penetration into the denser regions.

Figures 2.3-2.6 show comparisons of some results of the revised NRL model with similar calculations by EB. In these computations, the 1961 Chamberlin[25] model atmosphere is used, and N_2, O_2, and O are included as constituents. In the EB results, monoenergetic protons with isotropic pitch angle distributions are considered, whereas monoenergetic protons with a single pitch angle are treated in the NRL

results. Depositions in the polar regions are considered in both cases. Figures 2.3-2.6 present comparisons of the total ionization produced per unit volume versus altitude at several incident energies.

It can be seen in these Figures that the EB results at the lower energies can be matched very well at the lower altitudes by varying the pitch angle. At higher altitudes, there is some disagreement, especially for the 1000 keV calculation. The large differences for a 1000 keV proton are suggestive of a significant difference in the models used by EB and by NRL. Further study of References 9 and 25 indicated that the cross section for the process

$$H^+ + X \rightarrow H^+ + X^+ + e, \qquad (2.12)$$

i.e., direct ionization by protons, was not included in the EB calculations. At lower energies, charge exchange is the dominant process for ionization by protons, and the equilibrium fraction of hydrogen atoms is much larger than for protons; hence, this is a reasonable approximation at lower energies. At higher energies charge exchange cross sections are greatly reduced, the equilibrium fraction of protons is large, and the contribution from direct ionization is very significant.

To check whether this was indeed the case, the depositions were recomputed with the cross sections for the processes given by Eq. (2.12) set equal to zero. By then redefining the total number of charged particles at a given altitude as the sum of the N_2^+, O_2^+, and O^+ ions plus the number of protons generated from the charge exchange cycle, a new set of results was obtained. These results are shown in Figures 2.7-2.10.

It is seen that for energies of 100 keV or less, the agreement with EB is still good. In Figure 2.7, adding the charge exchange protons greatly overestimates the peak of the curve by about 50 per cent, whereas agreement is very good without this contribution. As noted in the previous section, however, the cross sections were extrapolated to very low energies, and this is probably the major source of the discrepancy. (The results in Figure 2.7 for total ions only are the same as the results in Figure 2.3. This follows from the fact that at 3 keV, the equilibrium fraction of hydrogen atoms is approximately unity; i.e., direct ionization by protons is effectively turned off.) Agreement is good for either calculation at 30 keV and 100 keV, as might be expected since this is the energy regime where charge exchange is dominant. The notably better agreement occurs at 1000 keV, as may be seen by comparing Figures 2.6 and 2.10. While the agreement in Figure 2.10 is not totally satisfactory, it is much better than that represented by Figure 2.6 and appears to verify the assumption that the proton direct ionization process is omitted by EB. The remaining discrepancies are probably due to differences in cross-section data.

The results presented thus far have involved only monoenergetic proton depositions. The program also treats a distribution of proton energies. An input flux with the energy distribution shown in Figure 2.11 was inserted into the program, and the results for total ionization produced as a function of altitude are shown in Figure 2.12. In this calculation, the Chamberlin 1961 atmosphere was again used, although it is possible to use any given model atmosphere.

Results given in this report have dealt only with ionization produced by proton depositions. However, it is possible to calculate the creation of other excited states or emission lines by putting in the relevant cross sections. For example, the calculation of the N_2 + 3914 angstrom emission line can be calculated by using the McNeal-Birely[20] data for this cross section.

The deposition model can be applied to deposition of energetic ions in debris particles such as that associated with STARFISH. In the coming year work will be done in this regard.

TABLE 2.1 - ELECTRON IMPACT CROSS SECTIONS FOR N_2

STATE	REFERENCES
Ionization	Rapp and Englander-Golder[26]; Schram, et al.[27]
$A^3\sum_u^+$	Borst[28]
$B^3\Pi_g$	Chung and Lin[30]; Stanton and St. John[29]
$C^3\Pi_g$	Finn, Aarts, and Doering[31]; Aarts and de Heer[32]
$W^3\Delta_u$	Chung and Lin[30]; normalized to Chutjin, et al.[33]
Vibrational	Schulz[35]; normalized to Spence, Mauer, and Schulz[36]
$a^1\Pi_g$	Green and Stolarski[34]
$b^1\Pi_u$	Green and Stolarski[34]
$b^1\sum_u^+$	Green and Stolarski[34]
Rydbergs	Green and Stolarski[34]

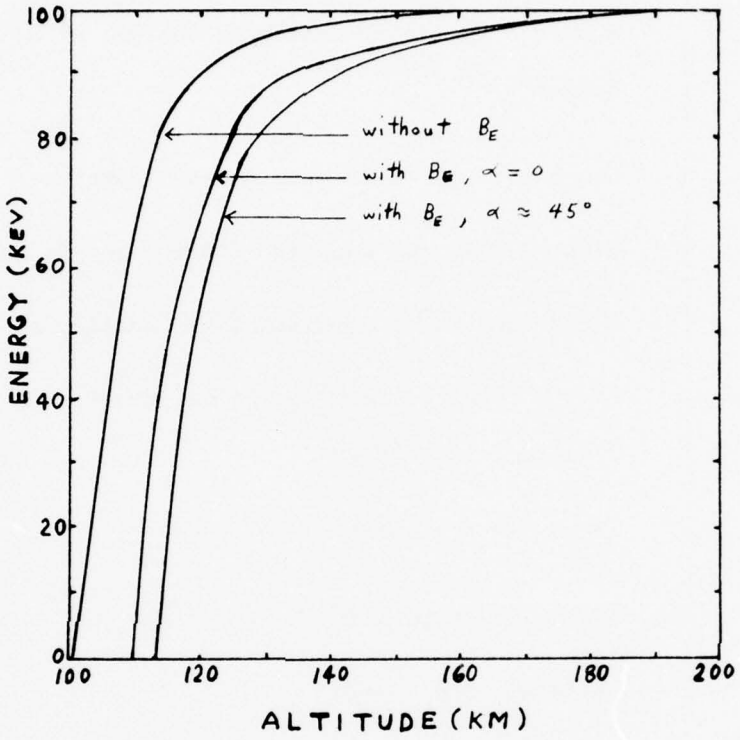

Fig. 2.1 — Comparison of 100 keV proton energy degradation in a pure N_2 atmosphere with and without the geomagnetic field B_E. α is the proton pitch angle with respect to the field lines.

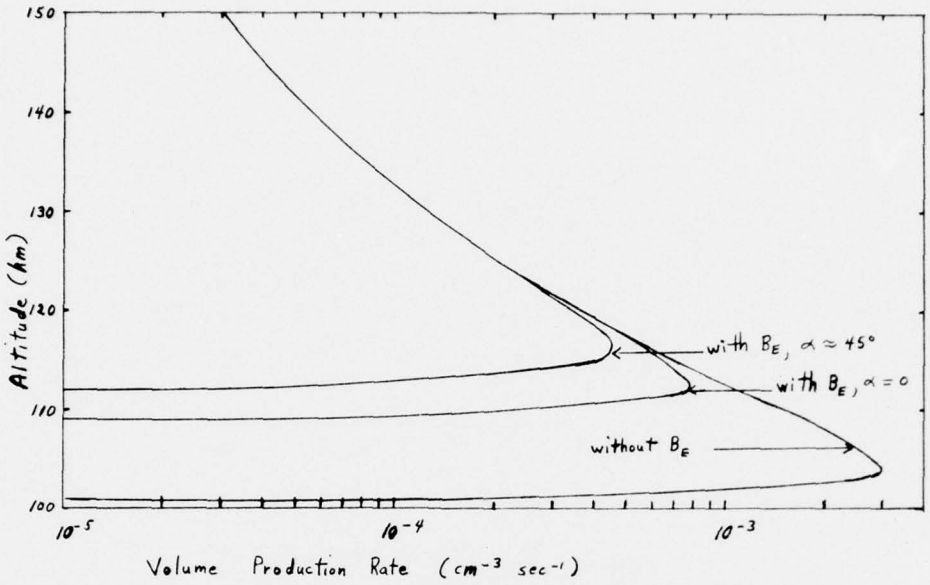

Fig. 2.2 — Number of ions produced vs altitude with and without the geomagnetic field B_E by deposition of a 100 keV proton in a pure N_2 atmosphere. α is the pitch angle.

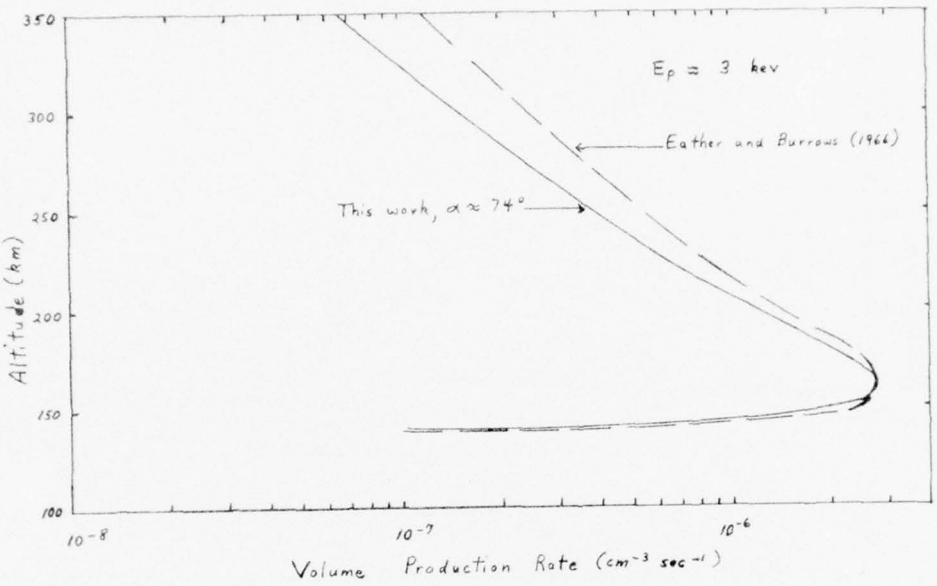

Fig. 2.3 — Number of ions produced by a 3 keV proton as a function of altitude in a Chamberlin 1961 model atmosphere

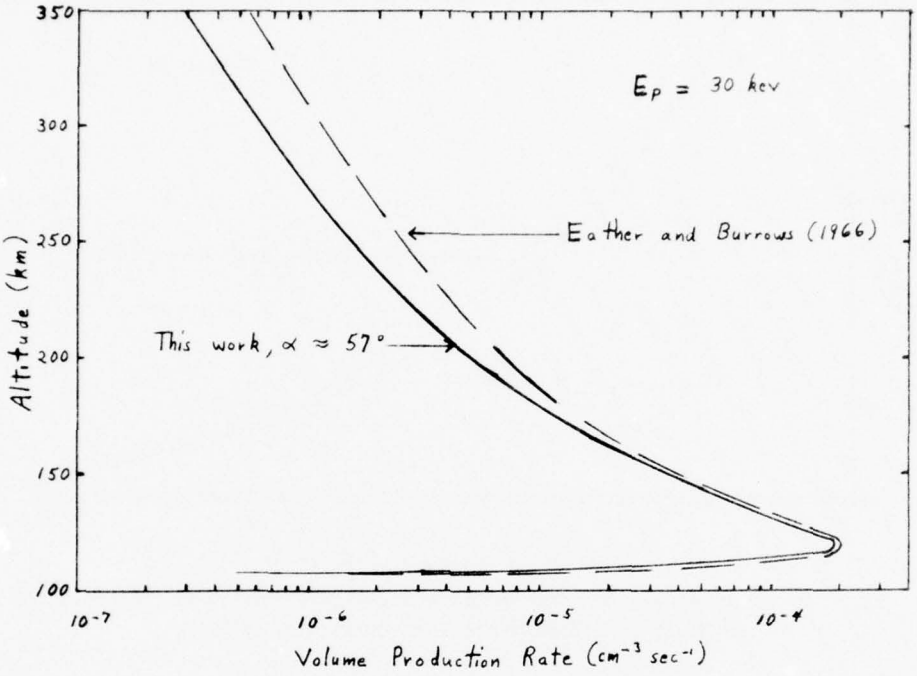

Fig. 2.4 — Number of ions produced by a 30 keV proton as a function of altitude in a Chamberlin 1961 model atmosphere

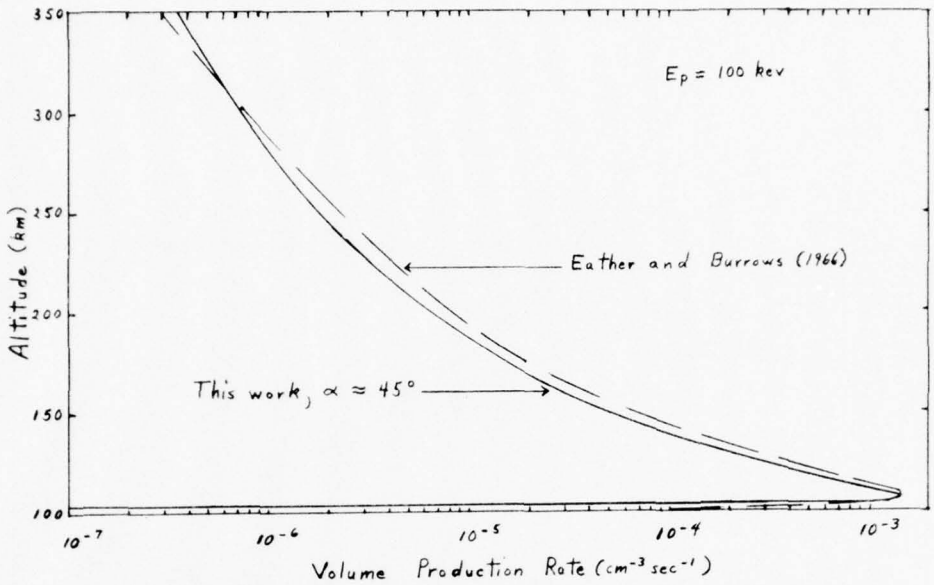

Fig. 2.5 — Number of ions produced by a 100 keV proton as a function of altitude in a Chamberlin 1961 model atmosphere

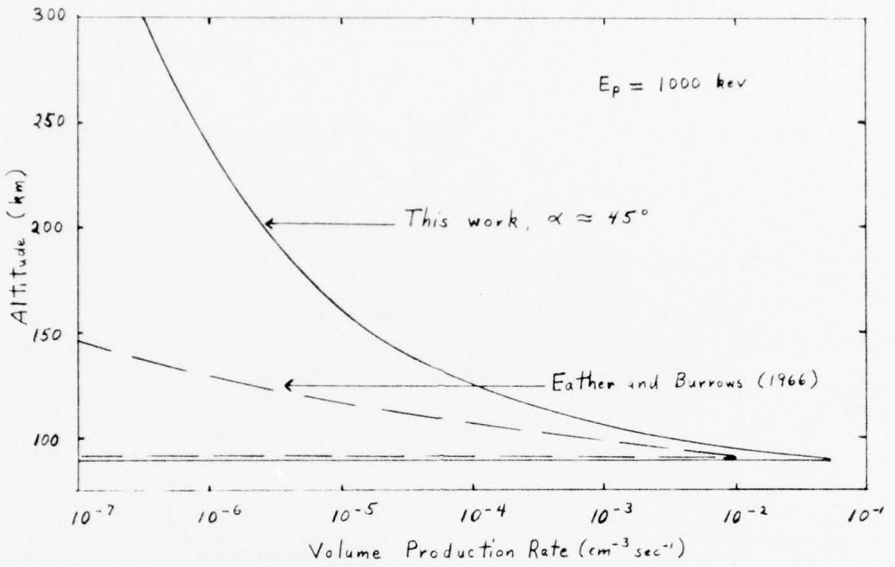

Fig. 2.6 — Number of ions produced by a 1000 keV proton as a function of altitude in a Chamberline 1961 model atmosphere

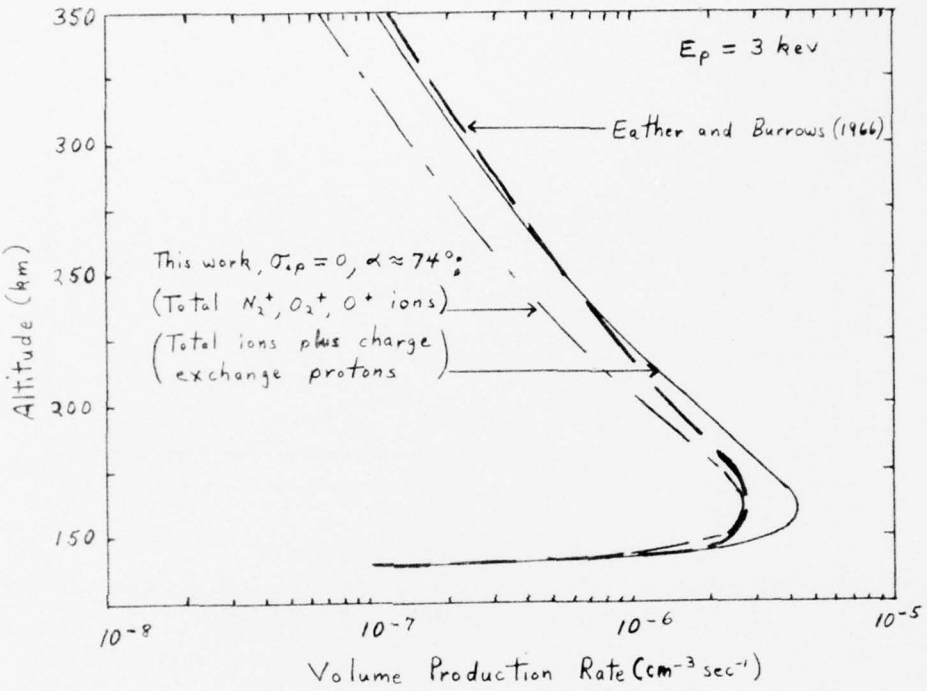

Fig. 2.7 — Recalculation of the ionization produced by a 3 keV proton in a 1961 Chamberlin model atmosphere when the cross section σ_{ip} for direct ionization by protons is set equal to zero

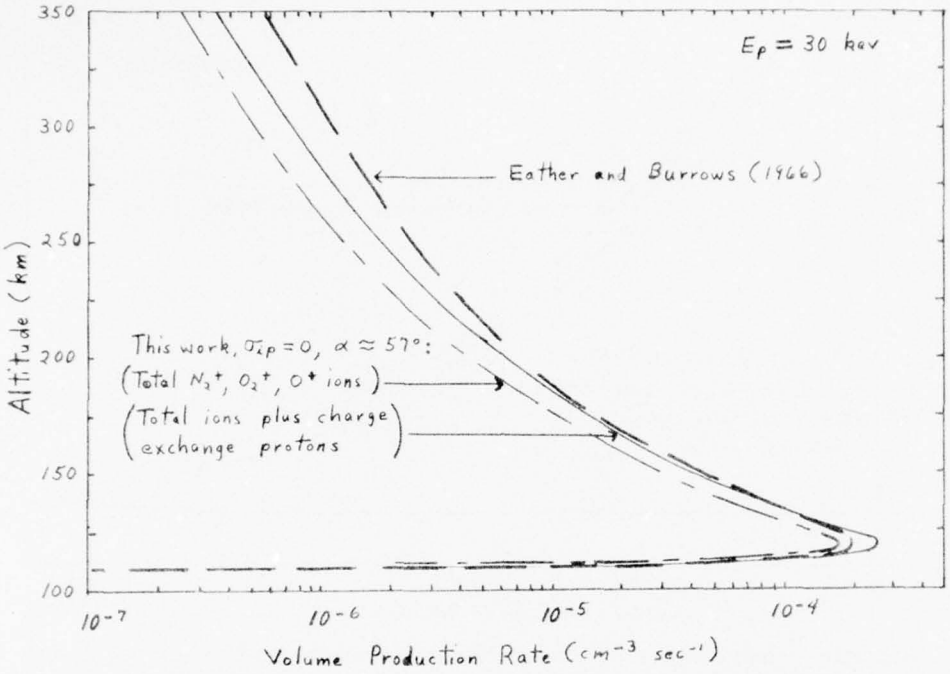

Fig. 2.8 — Recalculation of the ionization produced by a 30 keV proton in a 1961 Chamberlin model atmosphere when the cross section σ_{ip} for direct ionization by protons is set equal to zero

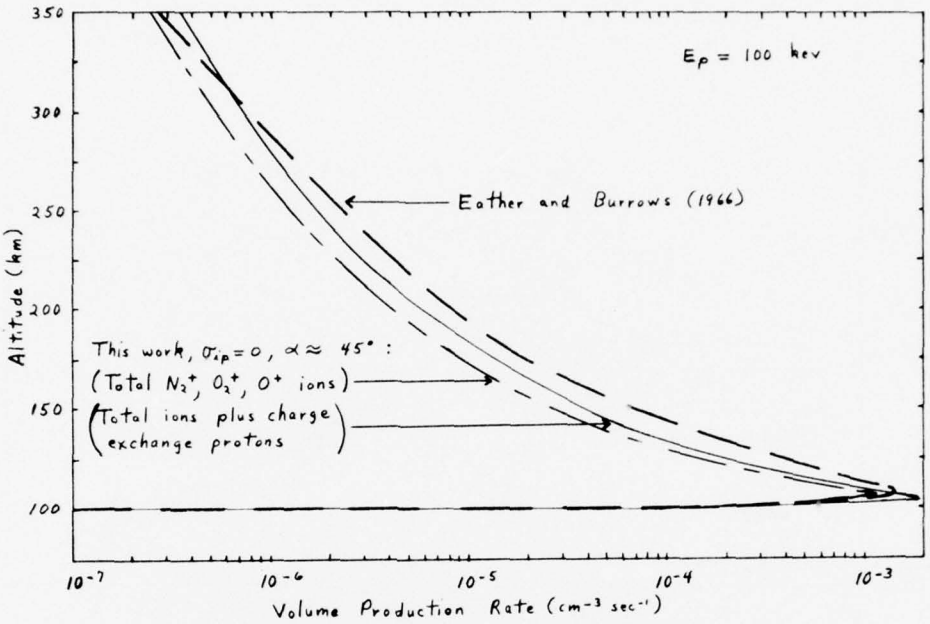

Fig. 2.9 — Recalculation of the ionization produced by a 100 keV proton in a 1961 Chamberlin model atmosphere when the cross section σ_{ip} for direct ionization by protons is set equal to zero

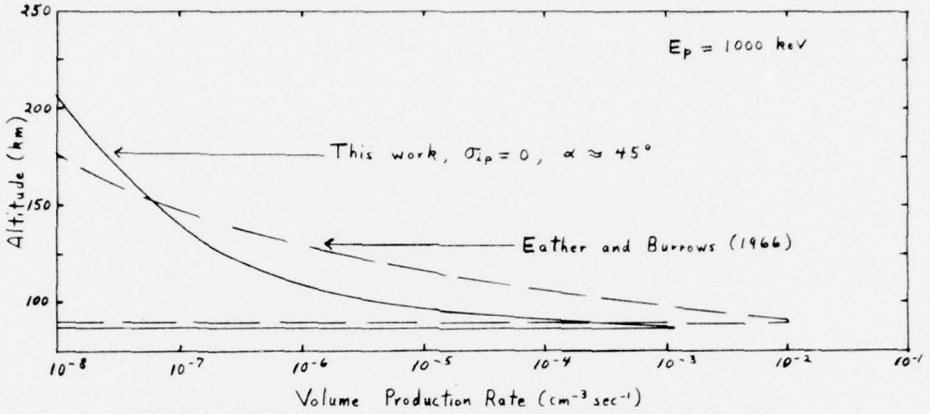

Fig. 2.10 — Recalculation of the ionization produced by a 1000 keV proton in a 1961 Chamberlin model atmosphere when the cross section σ_{ip} for direct ionization by protons is set equal to zero

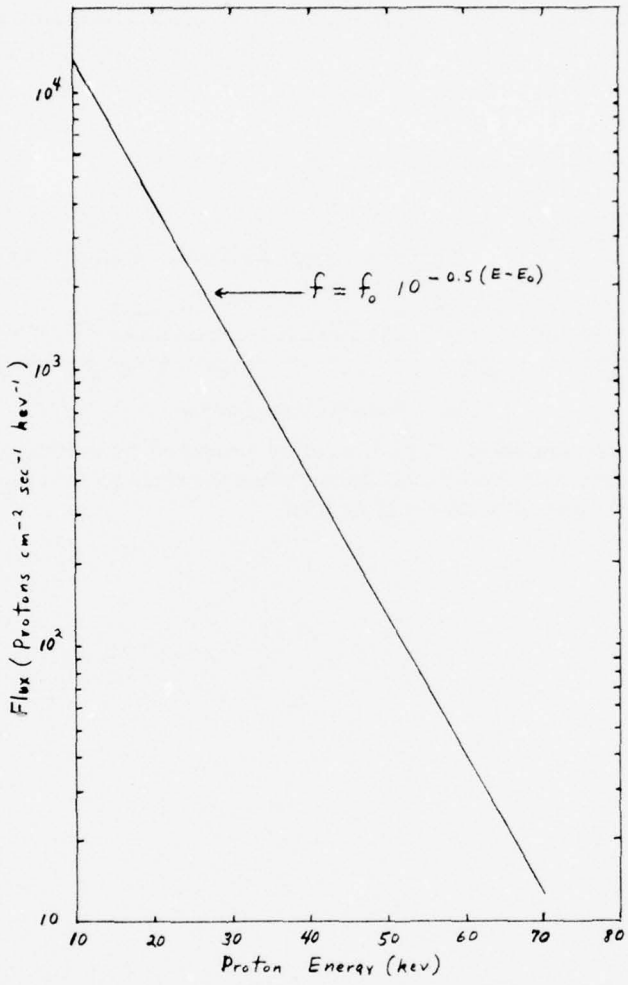

Fig. 2.11 — Proton energy distribution used in calculating the ionization vs altitude curve shown in Fig. 2.12

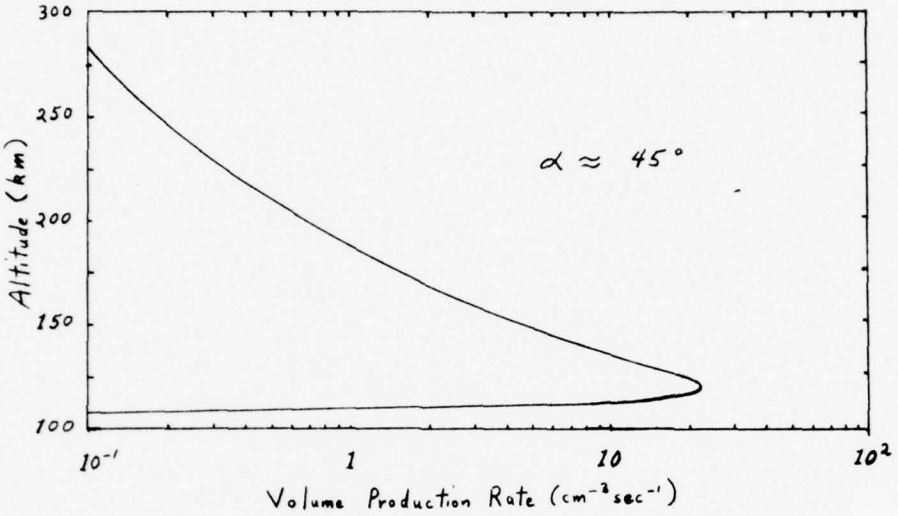

Fig. 2.12 — Ionization vs altitude in a Chamberlin 1961 atmosphere by proton flux of Fig. 2.11

Section 3

TRANSPORT TECHNIQUES FOR DESCRIBING THE ELASTIC SCATTERING OF ENERGETIC ELECTRONS

D. J. Strickland and I. B. Bernstein

In the past year, a code has been developed at the Naval Research Laboratory which solves an equation of transfer for energetic electrons.[43] The code is being applied to auroral studies and determines, for a given incident auroral electron spectrum, the electron flux as a function of pitch angle, energy, and altitude. The backscattered flux near 180° is very sensitive to the detailed angular dependence of the cross sections. In spite of the fact that the cross sections for large scattering angles are orders of magnitude smaller than for angles close to zero degrees, changes in the cross sections at large scattering angles produce noticeable changes in backscatter. To investigate such angular behavior in detail, we have applied the program to a simpler problem, that of purely elastic scattering by one constituent. The accuracy of the results is easier to determine for this case.

We begin by discussing the equation of transfer or Boltzmann equation for elastic scattering. This is followed by introducing a cutoff angle for a single scattering in order to study the importance of large angle scattering. Next, the Fokker-Planck equation for elastic scattering is introduced since it is derivable from the equation of transfer. Both numerical and analytic solutions have been obtained for the equation of transfer, and analytic solutions have been obtained for the Fokker-Planck equation. A subsection is devoted to discussing these

methods of solution. Finally, selected results for the two equations are presented followed by our conclusions.

3.1 METHODS

We wish to describe electron distribution functions which may possess strong anisotropies. The Boltzmann equation provides a starting point for such an exercise but in its most general form is not practical for most applications due to its complexity. There are several simplified versions of this equation which have had extensive use over the years, especialiy in the area of plasma physics. Of these we shall consider two here, the Boltzmann equation for infinitely massive scatterers and the counterpart Fokker-Planck equation, both for the case of elastic scattering alone.

We begin with the Boltzmann equation governing the distribution function f for elastic scattering by infinitely heavy scatterers:

$$\frac{\partial f}{\partial t} + \underline{v}\cdot\nabla_r f - \frac{e}{m}\left(\underline{E} + \frac{1}{c}\,\underline{v}\times\underline{B}\right)\cdot\nabla_v f = n\int d\Omega\,\sigma\,(v,\Theta)v\left[f(f(\underline{r},\underline{v}'t)-f(\underline{r},\underline{v},t)\right] \tag{3.1}$$

where n is the density of scatterers, σ is the differential cross section, and Θ is the scattering angle (see Fig. 3.1). Consider a steady state in the absence of electromagnetic fields where f depends on the space coordinate z alone. Eq. (3.1) then reduces to

$$\mu\,\frac{\partial}{\partial z}\,vf(z,v) = n\int d\Omega\,\sigma(v,\Theta)v\left[f(z,\underline{v}') - f(z,v)\right] \tag{3.2}$$

where μ is the cosine of the pitch angle ($\mu = \underline{v}\cdot\hat{e}_z/v$). Define the total cross section

$$\sigma_o = \int d\Omega\,\sigma \tag{3.3}$$

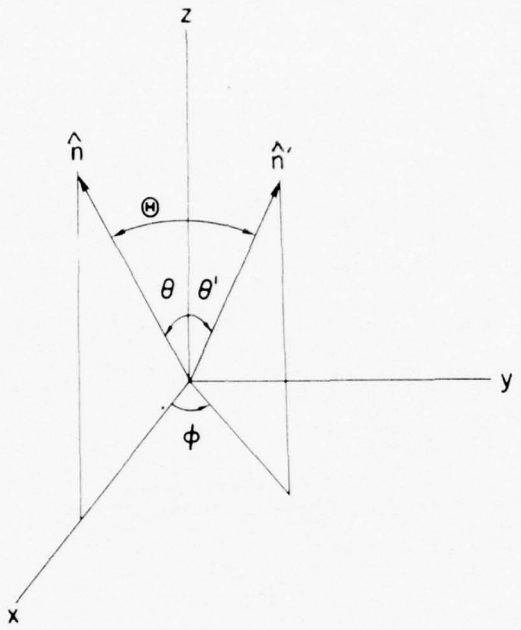

Fig. 3.1 — Geometry for the scattering of a particle from direction $\hat{n}'$ to $\hat{n}$ referenced to fixed direction z

and the differential scattering depth

$$d\tau = n\sigma_o dz \ . \tag{3.4}$$

Assuming azimuthal symmetry in f, Eq. (3.2) then yields

$$\mu \frac{\partial f}{\partial \tau} = \int d\mu' \ R(\mu, \mu') \ [f(\tau,\mu') - f(\tau,\mu)] \tag{3.5}$$

which is conventionally termed the equation of transfer.

The kernel R is

$$R(\mu,\mu') = \int_o^{2\pi} d\phi \ \sigma(v,\Theta)/\sigma_o \ . \tag{3.6}$$

Consider the case of the screened Coulomb cross section

$$\sigma(v,\Theta) = \frac{z^2e^4}{v^2p^2} \ \frac{1}{(1-\cos\Theta + 2\eta)^2} \tag{3.7}$$

with screening parameter η .[44,45]

On introducing

$$\cos\Theta = \underline{v}\cdot\underline{v}'/v^2 = \mu\mu' + \sqrt{1-\mu^2}\sqrt{1-\mu'^2}\cos\varphi \tag{3.8}$$

R becomes

$$R(\mu,\mu') = \frac{2\eta(1+\eta)(1+2\eta-\mu\mu')}{[(\mu-\mu')^2 + 4\eta(1-\mu\mu') + 4\eta^2]^{3/2}} \tag{3.9}$$

Consider next a cutoff angle Θ_c such that for larger values of the scattering angle Θ,σ is set to zero. The parameter Θ_c enables us to examine the dependence of f on large angle scattering. In terms of this modified cross section, R is

$$R(\Theta_c,\mu,\mu') = \frac{2\eta(1 + 2\eta-\mu_c)}{\pi(1 - \mu_c)} \quad \frac{1}{a^2-b^2} \quad \cdot$$

$$\left[\frac{-b\sin\varphi_{max}}{a + b\cos\varphi_{max}} + \frac{2a}{\sqrt{a^2-b^2}} \tan^{-1}\left(\frac{\sqrt{a^2-b^2}}{a + b} \tan\frac{\varphi_{max}}{2}\right)\right] \tag{3.10}$$

where $a = 1 + 2\eta - \mu\mu'$, $b = \sqrt{1-\mu^2}\sqrt{1-\mu'^2}$, $\mu_c = \cos\Theta_c$, and φ_{max} is the maximum allowed azimuthal angle for given Θ_c, μ and μ'. (See Appendix A for further details).

To solve Eq. (3.5), the range in μ has been divided into N zones, and the flux has been given a piece-wise linear dependence over the grid. The matrix representation of Eq. (3.5) is then

$$\mu_i \frac{\partial f_i}{\partial\tau} = \Sigma A_{ij} f_j \quad . \tag{3.11}$$

Examples of the dependence of R on Θ_c, μ and μ' are given in Fig. 3.2 for a value of η of 10^{-4}. Such a value would be appropriate for electrons in the 100 kilovolt range scattering off a light nucleus. The sharply-peaked behavior of R at small scattering angles suggests that one make a Fokker-Planck expansion of the collision integral in Eq. (3.2) (see, e.g. Bethe et al.[45] and Rosenbluth et al.[46]). The resulting equation [see Appendix B] is

$$\mu \frac{\partial f}{\partial\tau} = \frac{Q}{2\sigma_o} \frac{\partial}{\partial\mu} \left[(1 - \mu^2) \frac{\partial f}{\partial\mu}\right] \tag{3.12}$$

where

$$Q = 2\pi\int_o^\pi d\Theta \sin\Theta (1 - \cos\Theta)\sigma(v,\Theta) \tag{3.13}$$

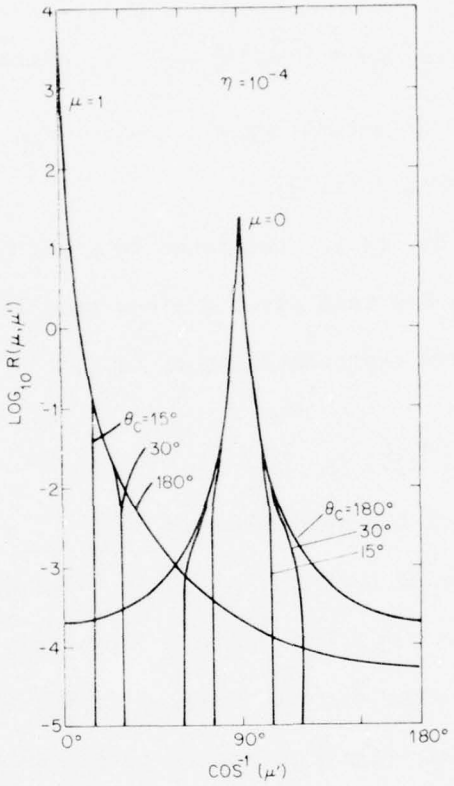

Fig. 3.2 — Plots of $R(\Theta_c, \mu, \mu')$ vs incident pitch angle for $\eta = 10^{-4}$ and for the two resultant pitch angles $\cos^{-1} \mu = 0$ and 90°

is the momentum transfer cross section. For the screened coulomb potential

$$\frac{Q}{2\sigma_o} = \eta \left[(1+\eta) \ln \frac{(1+\eta)}{\eta} - 1 \right]. \tag{3.14}$$

In our finite difference approximation to Eq. (3.12), the right hand side is represented by

$$\frac{Q}{2\sigma_o} \Delta\mu^2 \left[(1-\mu^2_{i-\frac{1}{2}})(F_{i-1}-f_i) - (1-\mu^2_{1+\frac{1}{2}})(f_i-f_{i+1}) \right] \tag{3.15}$$

at interior points, and by

$$\frac{-Q}{\sigma_o \Delta\mu} (f_1-f_2) \qquad (\mu = 1) \tag{3.16}$$

$$\frac{Q}{\sigma_o \Delta\mu} (f_{N-1} - f_N) \qquad (\mu = 1) \tag{3.17}$$

where the domain in μ has been divided into N equal intervals and $\mu_{i-\frac{1}{2}}$ is the value of μ half-way between μ_{i-1} and μ_i. We have further multiplied the terms corresponding to $\mu = \pm 1$ by $(1 - \Delta\mu/4)$ for reasons explained at the end of this section.

Both numerical and analytic methods have been used to solve the matrix equations. Specifically, both methods have been applied to the equation of transfer, and the analytic technique to the Fokker-Planck equation.

Physically, for a well posed problem one must stipulate the distribution function for those particles incident on the system; collisions then determine the properties of those particles that are emerging. For the case here considered this corresponds to stipulating $f(o,\mu)$ for $1 \geq \mu > 0$ and $f(\tau_o,\mu)$ for $0 > \mu \geq -1$. In the work here

presented the choice for all cases was $f(\tau_o,\mu) = 0$, $0 > \mu \geq -1$, corresponding to an absorbing boundary.

The solutions obtained by numerical integration are based on an iteration scheme as follows: First, for $0 < \mu_i \leq 1$, $f_i(\tau)$ is set to zero and using a second order predictor-corrector scheme, Eq. (3.11) is integrated forward to $\tau = \tau_o$ (the lower boundary) for $0 < \mu_i \leq 1$ and in the process the results are stored on a pre-specified grid in τ. Eq. (3.11) is then integrated backwards to $\tau = 0$ for $0 < \mu \geq -1$ using the values of $f_i(\tau)$ just computed for $0 < \mu_i < 1$, and just as with the forward integrations, the results are stored on the same grid in τ. Forward and reverse integrations proceed until the values of $f_i(\tau)$ do not change appreciably. In practice, a technique is used which projects the iterated values of f_i to their converged values in only three or four iterations.

We have used a standard eigenvalue method to obtain the analytic solutions of the difference differential equations. Assuming f_i can be represented by $\psi_i e^{-\lambda\tau}$ we solve the characteristic equation

$$\sum_j \left(\frac{A_{ij}}{\mu_i} - \lambda \delta_{ij} \right) \psi_j = 0 \qquad (i = 1,N) \tag{3.18}$$

leading to

$$f_i(\tau) = \sum_\ell C_\ell \psi_{i\ell} e^{-\lambda_\ell \tau} \qquad (\ell = 1,N) \tag{3.19}$$

where λ_ℓ is the ℓ^{th} eigenvalue, $\psi_{i\ell}$ is the ℓ^{th} eigenfunction at μ_i, and C_ℓ is a coefficient determined by boundary conditions.

By inspection, one can verify that the following is also a solution to either the equation of transfer or the Fokker-Planck equation:

$$f_i = \alpha + \beta \left(\mu_i - \frac{Q}{\sigma_o} \tau \right) \tag{3.20}$$

where α and β are constants (for further details see Bethe et al.).

It turns out that two of the eigensolutions to the discretized equations serve to represent this solution, namely those with eigenvalue which go to zero as $N \to \infty$. In order to minimize errors for $\tau_o \gg 1$ associated with approximating the exact solution (Eq. 3.20) by a sum of exponentials, it is convenient to suppress the two eigensolutions corresponding to the smallest eigenvalues and write

$$f_i = \alpha + \beta \left(\mu - \frac{Q\tau}{\sigma_o} \right) + \sum_{\ell = 1}^{N-2} C_\ell \psi_{i\ell} e^{-\lambda_\ell \tau} \tag{3.21}$$

If one seeks eigensolutions $\phi_\ell(\mu) e^{-\lambda_\ell \tau}$ to Eq. (3.12), they satisfy

$$\lambda_\ell \mu \phi_\ell = \frac{d}{d\mu} \left[(1 - \mu^2) \frac{d}{d\mu} \phi_\ell \right] \tag{3.22}$$

from which it follows that

$$\lambda_\ell \int_{-1}^{+1} d\mu \, \mu \phi_\ell = \int_{-1}^{+1} d\mu \, \frac{d}{d\mu} \left[(1 - \mu^2) \frac{d\phi_\ell}{d\mu} \right] = 0. \tag{3.23}$$

Hence, eigensolutions of the differential equation carry no current.[45]

To enhance the correspondence between eigensolutions to the Fokker-Planck matrix equation and Eq. (3.12), the former are made to satisfy condition (3.23) in the form

$$y_1 + 2 \sum_{i=2}^{N-1} y_i + y_N = 0 \qquad (3.24)$$

where y_i within the sum is given by our finite difference approximation to the right hand side of Eq. (3.22) (see Eq. (3.15)). Equation (3.24) then specifies y_1 and y_N and leads to the replacement of Eqs. (3.16) and (3.17) by

$$\text{RHS} = -\frac{Q}{\sigma\Delta\mu}\left(1 - \frac{\Delta\mu}{4}\right)(\phi_1 - \phi_2) \quad (\mu = 1) \qquad (3.25)$$

$$= \frac{Q}{\sigma\Delta\mu}\left(1 - \frac{\Delta\mu}{\mu}\right)\left(\phi_{N-1} - \phi_N\right) \quad (\mu = -1) \qquad (3.26)$$

3.2 RESULTS

In this section, we present solutions of the equation of transfer and of the Fokker-Planck equation for a variety of conditions. Values of 10^{-3} and 10^{-4} for the screening parameter are considered, which would apply to kilovolt electrons scattering off light nuclei. A wide range of total scattering depths τ_o is assumed, from values of 5 to 1000. Values of the cutoff angle Θ_c of 15°, 30° and 110° have been used in the equation of transfer. Finally, incident fluxes with both isotropic and Gaussian dependences have been assumed.

Figs. 3.3 and 3.4 demonstrate the sensitivity of the back-scattered flux to $\sigma(\Theta,\eta)$ at large pitch angles. The solutions were obtained with the equation of transfer. The screening parameter is 10^{-4} for results in Figs. 3.3 and 10^{-3} for those in Fig. 3.4, thus providing for much stronger forward scattering for the first set of results. The total scattering depth τ_o is 100 for both systems. In each figure, results are given at $\tau = 0$ and 50 for Θ_c values of 180°,

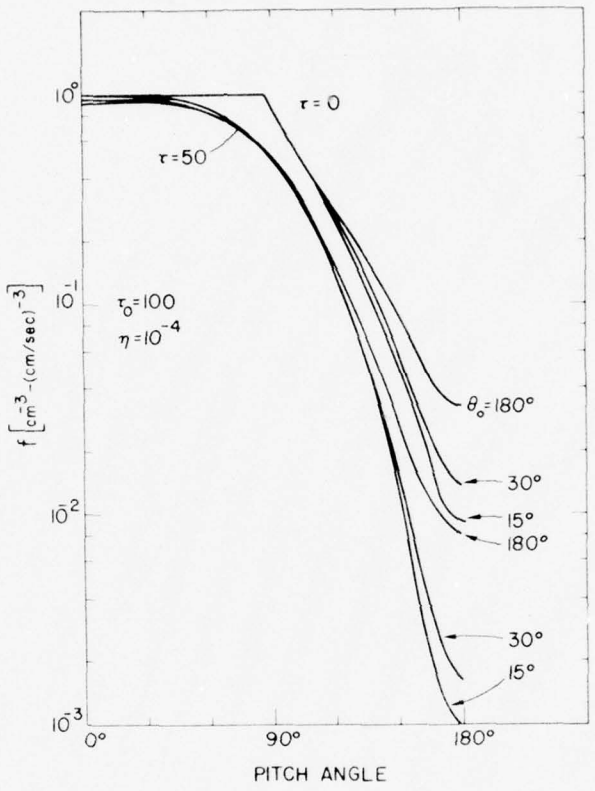

Fig. 3.3 — Solutions to the equation of transfer at the upper boundary and halfway through the medium for cutoff angles Θ_c of 180°, 30°, and 15° and for $\eta = 10^{-4}$

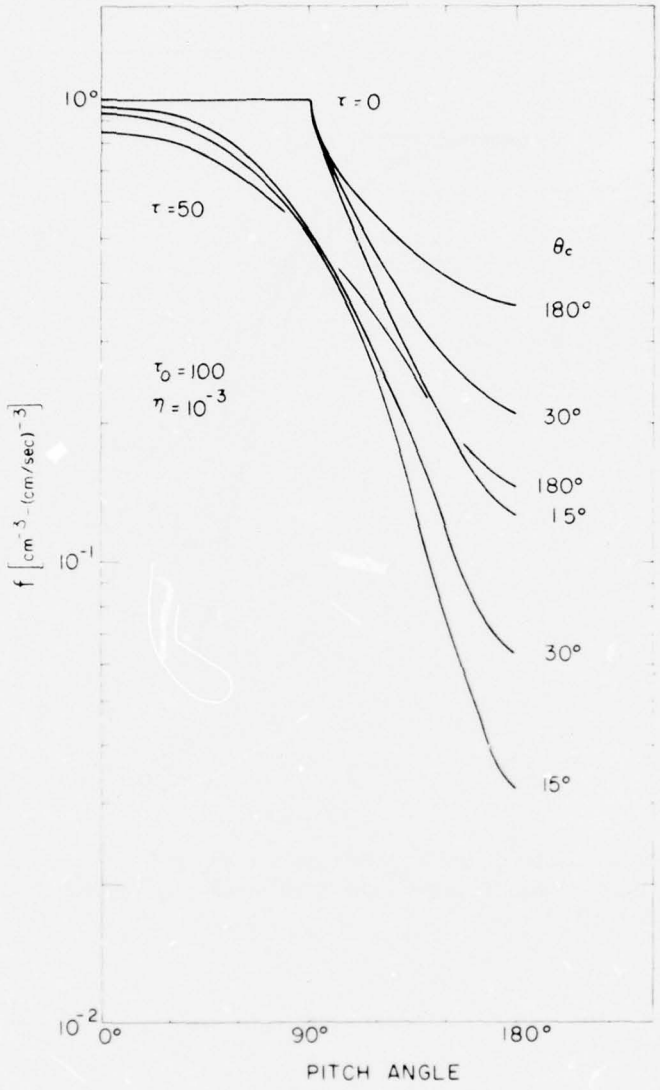

Fig. 3.4 — Solutions similar to those in Fig. 3.3, but with $\eta = 10^{-3}$

30° and 15°. We remind the reader that scattering is restricted to values less than or equal to the chosen value of Θ_c. The backscattered flux near 180° does decrease significantly as large angle scattering is restricted in spite of the fact that the values of the cross sections being affected are extremely small (see Fig. 3.2 for $\eta = 10^{-4}$). The results can be explained in terms of the effective turning point for the particle. Once the particle does turn, its probability of directly escaping through the upper boundary goes as exp $(-\tau)$ where τ is the depth from this turning point to the boundary. A small change in τ arising from varying Θ_c produces a much larger change in the escape probability, which then reflects itself in the backscattered flux. The results in Figs. 3.3 and 3.4 lead to an important point -- namely that a detailed knowledge of the scattering cross section is essential to accurately predict backscatter for systems with τ_o not much greater than 1. The Fokker-Planck solutions exhibit a similar sensitivity to Θ_c through changes that occur in the momentum transfer cross section.

Figs. 3.5 and 3.6 give fluxes at $\tau = 0$ for $\eta = 10^{-3}$ and for $5 \leq \tau_o \leq 1000$. Since all results refer to the same value of η, the ratio of the total number of scatterers for any two situations is simply the ratio of the corresponding values of τ_o. The incident flux is isotropic in Fig. 3.5 and assumes a Gaussian dependence $[\exp (-1-\mu)^2/.25)]$ in Fig. 3.6. For each case, solutions have been obtained to both the integral equation and its counterpart Fokker-Planck equation and are presented in these figures. As τ_o increases,

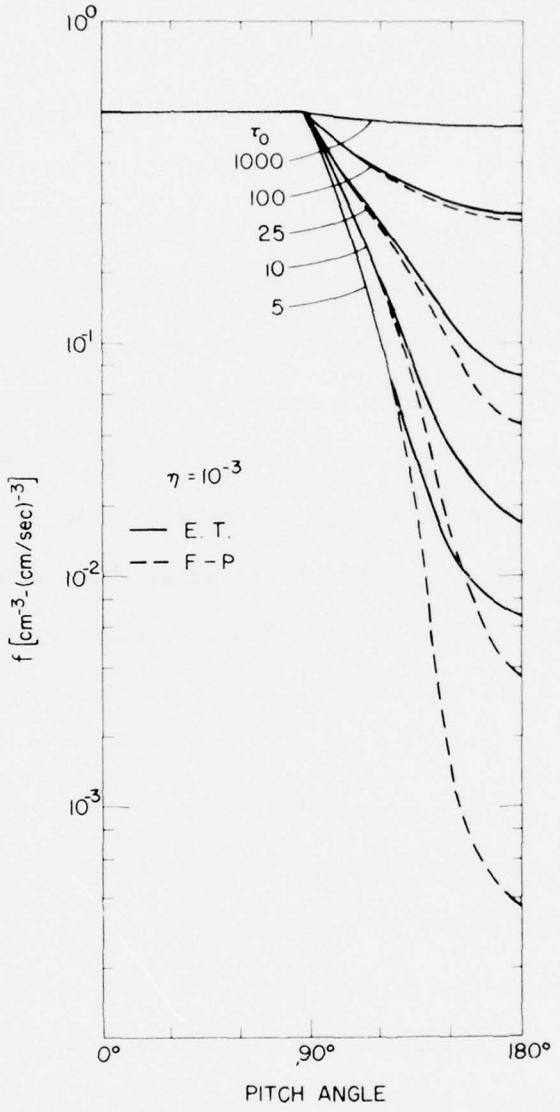

Fig. 3.5 — Transfer solutions and Fokker-Planck solutions for an isotropic incident flux and a range of total depth τ_o

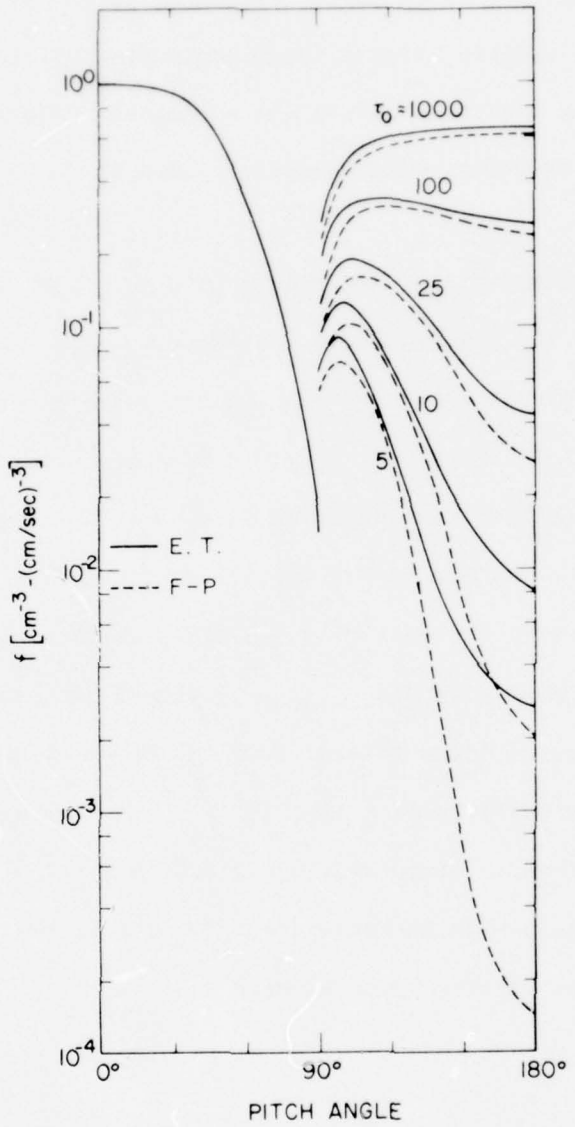

Fig. 3.6 — Solutions similar to those in Fig. 3.5 except with an incident flux having the Gaussian dependence exp $(-(1-\mu)^2)/.25$

the albedo or ratio of total backscatter to total incident flux approaches unity. Results for both equations are in good agreement for systems with $\tau_o \geq 100$. For such cases, enough scatterers are present for multiple small angle scattering to be effective. With decreasing τ_o, however, single large angle scattering becomes relatively more important and is not adequately described by the Fokker-Planck equation, which underestimates the true amount of backscatter.

The variation of the flux with τ is shown in Fig. 3.7 for $\eta = 10^{-3}$, $\tau_o = 10$, and isotropic incidence. Again, solutions to both equations are given. Since we are considering a rather thin system, the incident flux experiences very little attenuation. The solution at $\tau = 10$ illustrates the lower boundary condition: zero flux from below. A second example of the variation of the flux with τ is shown in Fig. 3.8. Here, the system is ten times thicker and the incident flux has a Gaussian dependence on μ. Fokker-Planck solutions are not included because of the number of curves already presented. Their behavior can be fairly well estimated from considering the previous figures. The imposed minimum at $\tau = 0$ due to the incident profile rapidly disappears with increasing τ. For $\tau \geq 5$, the flux becomes a monotonically decreasing function with μ.

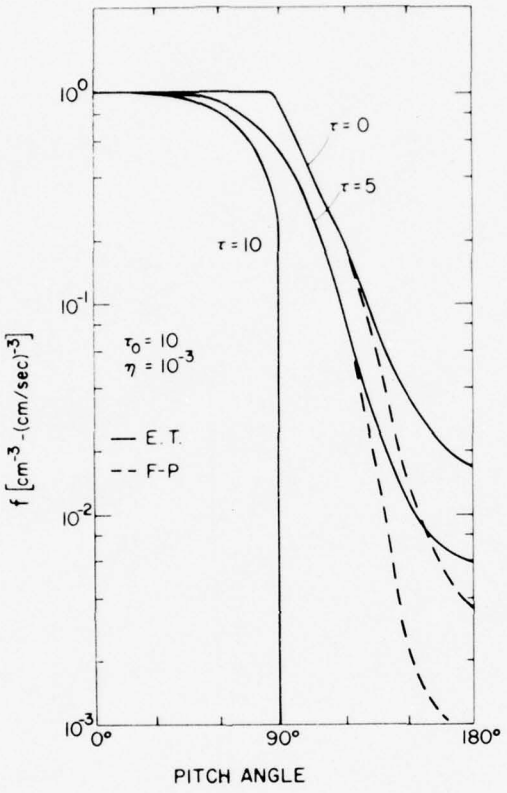

Fig. 3.7 — Transfer solutions and Fokker-Planck solutions for an isotropic incident flux showing their variation with depth τ

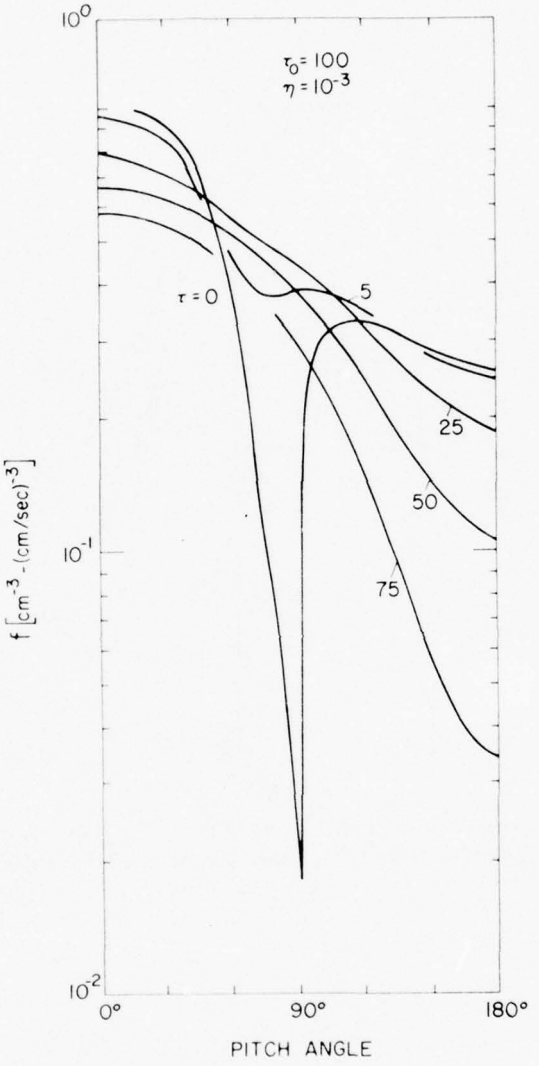

Fig. 3.8 — Transfer solutions for an incident flux with Gaussian dependence given in Fig. 3.6 showing their variation with depth τ

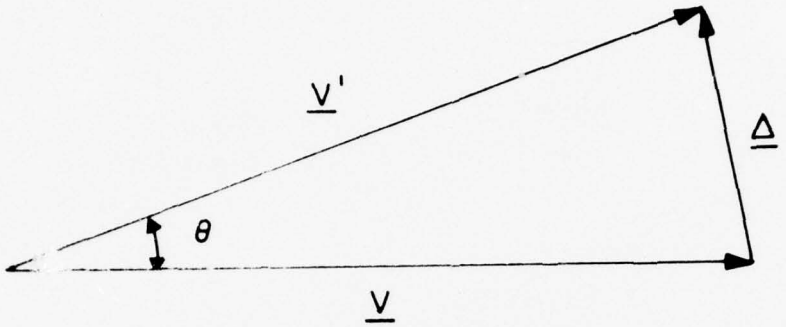

Fig. 3.9 — Relationship between incident velocity $\underline{v}$ and resultant velocity $\underline{v}' = \underline{v} + \Delta$. The case treated is for elastic scattering, i.e. $v' = v$.

Table 3.1. $(Q/2\sigma_o)$ from Eq. (3.14) versus Screening Parameter η.

η	$Q/2\sigma_o$
10^{-2}	3.6×10^{-2}
10^{-3}	5.9×10^{-3}
10^{-4}	8.2×10^{-4}

Section 4

AURORAL CHEMISTRY -- NO

E. Hyman, D. J. Strickland,
P. S. Julienne and D. F. Strobel

A most intriguing aeronomical problem in recent years is the anomalously large enhancements of NO concentration that have been inferred from measured $[NO^+]/[O_2^+]$ ratios[47-49]; [Swider and Narcisi, 1970; 1974] and directly measured[50] in auroral arcs. (The analysis of Jones and Rees[51] suggests that a measurement of the $[NO^+]/[O_2^+]$ ratio is not necessarily an accurate means to infer the NO density at the time of the measurement.) The available evidence suggests that these enhancements are spatially and temporally restricted to auroral arcs. There is considerable variability in the peak NO densities; for example, Swider and Narcisi[49] infer $[NO] \sim 6 \times 10^8$ cm^{-3} at 110 km whereas Zipf et al.[50] measured 3.8×10^{10} cm^{-3} at 120 km. It should be noted that other measurements on the latter rocket flight suggest [NO] was only $1\text{-}5 \times 10^{10}$ cm^{-3} at 110 km as compared with the mass spectrometer result of 2×10^{11} cm^{-3}.[51]

Attempts to deduce NO concentrations from studies of the deactivation of $N_2(A^3\Sigma_u^+)$ molecules[52] and from NO γ band emission[53] are not conclusive since the production mechanisms are not properly understood. In the former case the experimental cross sections adopted in the study were too high.[54] In the latter case it has not been demonstrated that auroral γ band emission is indicative of ambient NO concentrations.

The Zipf et al. measurements are thus the most perplexing observations to explain and appear to violate the principle of energy conservation if precipitating auroral primaries are the major energy source.[51] Previous theoretical studies of auroral events have addressed a broad range of auroral processes but have not specifically tackled the formidable problem of auroral NO.[51] In this paper we confine our attention to auroral NO and investigate the applicability and limitations of conventional midlatitude ionospheric chemistry and certain speculative chemical schemes to address the question of how much NO can be produced during an auroral event and how chemically this production can be maximized. We conclude that while localized enhancements of $[NO]$ to $\sim 10^{10}$ cm^{-3} are possible in a narrow altitude range, special and improbable circumstances are required; for example, vibrationally hot O_2.

4.1 CONVENTIONAL CHEMISTRY

First we discuss auroral NO production on the basis of conventional midlatitude chemistry, where odd nitrogen is formed by dissociation and ionization of N_2 with 9.8 and 15.6 eV required, respectively. In the case of N_2^+ production subsequent ion-molecule reactions are needed to break the N_2 bond, but these reactions are very exothermic. In either event considerable energy ($\geq$ 10eV) must be expended.

In the altitude range of interest, 100-120 km, N_2 is the dominant constituent and consequently the precipitating energetic electrons will dissipate most of their energy by dissociating and

ionizing N_2. There are three principal channels that must be considered and are illustrated in Figure 4.1. A direct ionization channel results in the production of N_2^+ which either reacts with O to form NO^+ and $N(^2D)$[55] or with O_2 to recycle N_2. For typical fluxes and auroral composition, 16% of the particle flux energy is expended to produce odd nitrogen by this channel. If $[NO] \sim [O]$ then N_2^+ would preferentially react with NO to give $NO^+ + N_2$ and cut off odd nitrogen production.

N_2 also dissociates in the manner described by Oran et al.[55] to produce $N(^2D) + N(^4S)$. Approximately 26% of the total energy is consumed in this channel. In addition 11% of the particle energy is used to dissociatively ionize N_2 and form N^+ and N. The electronic state of the N atom is not known but presumed, without serious consequences, to be in the ground ^4S state. The N^+ will react with O_2 to produce either NO^+ or $N(^2D)$. According to studies by Rusch et al.[56] and Strobel et al.[57], recent odd nitrogen data requires that NO^+ dissociatively recombine to form principally $N(^2D)$. Thus, the principal source of $N(^4S)$ is the pure dissociation channel.

The remaining ~ 50% of the energy is used to ionize O and O_2, to produce radiation, etc. Subsequent reactions of O_2^+ and O^+ do not produce odd nitrogen, except the minor reaction path $O^+ + N_2 \rightarrow NO^+ + N(^4S)$. In the region 100-120 km O^+ reacts preferentially with O_2 unless either O^+ is translationally hot and/or N_2 is vibrationally excited. The measured O^+ concentrations preclude the rapid removal of O^+ by a fast reaction path and imply that O^+ has less than 0.4 eV of translational energy and that the $v \geq 2$ vibrational

levels of N_2 have a Boltzmann distribution at the kinetic temperature.

In summary, the precipitating energetic electrons expend ~ 50% of their energy in the production of odd nitrogen. It takes about 10 eV to dissociate N_2 and about 20 eV to produce a pair of odd nitrogens, which is more efficient than the 35 eV required to produce an ion pair. Thus, while odd nitrogen is efficiently produced, substantial energy (10eV) is required to initiate its production. The chemistry outlined in Fig. 4.1 results in the production of 1.9 $N(^2D)$ atoms for each $N(^4S)$ atom. The molecular processes involved in N atom production are not sensitive to the environmental conditions in the auroral zone in a manner that would alter the $N(^2D)$ to $N(^4S)$ production ratio.

For $N(^2D)$ and $N(^4S)$ there are two major reaction paths: a fast reaction with NO and a slower reaction with O_2. In the case of $N(^2D)$ the reaction paths are comparable when $[NO]/[O_2] \sim 0.1$. Thus, until NO is built up to large concentrations $N(^2D)$ mostly reacts with O_2 to produce more NO. For $N(^4S)$ it is well known that its reaction with O_2 involves a substantial activation energy (~ 6 k cal) and at room temperature is very slow ~ 10^{-16} cm^3 sec^{-1}. The reaction paths of $N(^4S)$ are comparable when $[NO]/[O_2] \sim 4 \times 10^{-6}$; i.e., for NO concentrations below ambient values. Large buildups of NO are precluded in a short period of time under normal circumstances as much of the NO produced by $N(^2D) + O_2$ will be destroyed by $N(^4S) + NO$. It is obvious that to maximize the auroral NO production rate the appropriate chemistry must favor conversion of $N(^4S)$ into NO rather than N_2. Accordingly the reaction $N(^4S) + O_2$ must proceed at a rapid rate. The small steric

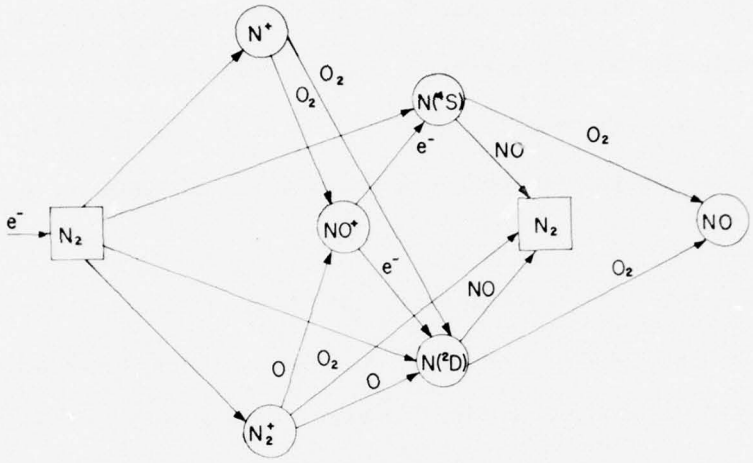

Fig. 4.1 — Principal odd nitrogen reactions leading to the formation of auroral NO

factor for this reaction eliminates the possibility of hot $N(^4S)$ atoms reacting with O_2 before being thermalized by collisions with the more abundant N_2 molecules. Electronic excitation of O_2 to $^1\Delta_g$ state does not help since the reaction $N(^4S) + O_2(^1\Delta_g) \rightarrow NO + O$ is slow [$< 3\times10^{-15}$ cm^3 sec^{-1}, Clark and Wayne[58]]. An examination of the reaction trajectory suggests that O_2 vibrational energy should be available to surmount the energy barrier. For sufficiently hot $O_2(v)$ $N(^4S)$ could react at a rate approaching 2×10^{-12} cm^3 sec^{-1} and $[NO]/[O_2] \sim 0.05$ would be the condition for equal probability of reaction with O_2 and NO.

Even with vibrationally hot O_2 in an auroral arc, the buildup of NO would terminate when $[NO]/[O_2] \geq 0.1$, since any additional $N(^4S)$ and $N(^2D)$ atom production would destroy rather than increase the NO concentration. At 120 km we estimate that NO could not exceed 5×10^9 cm^{-3} in contradiction to the mass spectrometer measurements of Zipf et al.[50] This upper limit [NO] estimate would have to be lowered if large amounts of O_2 were dissociated as the spectrometer results of Zipf et al. suggest. It should be emphasized that given sufficient time ($\gg 10^4$ seconds for a typical auroral arc) the NO concentration will build up to $0.1[O_2]$ if the $N(^2D)$ production rate exceeds that of $N(^4S)$ and if transport effects are not included.

4.2 THE MODEL

To make these estimates quantitative we have constructed an idealized model to describe the buildup of NO during auroral events. The model is described in detail in a technical report available from

the authors.[59] Production rates of ions, excited states, $N(^4S)$, $N(^2D)$, optical emission, etc., are generated by an energetic electron deposition code described in a technical report by Strickland et al.[60] The severity of the auroral NO problem allows us to neglect transport processes. Our model results may yield larger NO densities than measured as a consequence of this assumption. For initial values of odd nitrogen densities, the model of Strobel[61] was adopted; the results are insensitive to this choice. The time dependent continuity equations are integrated for all important constituents whose chemical time constant exceeds one second. Chemical equilibrium is assumed for constituents with chemical time constants less than one second. The important rate constants are tabulated in Table 4.1.

The model was applied to describe the remarkable auroral arc probed by Zipf et al. The energy deposition rate, illustrated in Fig. 4.2, was chosen to reproduce the measured 3914 Å intensity as a function of altitude. Under the most favorable conditions, $T_v(O_2) \geq$ 2 eV, the NO buildup as a function of time and altitude is illustrated in Fig. 4.2. According to Donahue[51] this auroral arc existed previous to the measurement for $\sim 4 \times 10^3$ seconds. Our model predicts a maximum $[NO] \sim 5 \times 10^9$ cm^{-3} with the enhancement localized in the 95-115 km region. To reach the NO cutoff density $\sim 0.1[O_2]$ requires buildup times $\gg 1\text{-}^4$ seconds.

The sensitivity of the model to various input parameters is illustrated in Fig. 4.3. The NO buildup is most sensitive to the O_2 vibrational temperature and the $N(^2D)$ branching ratio for $NO^+ + e$.

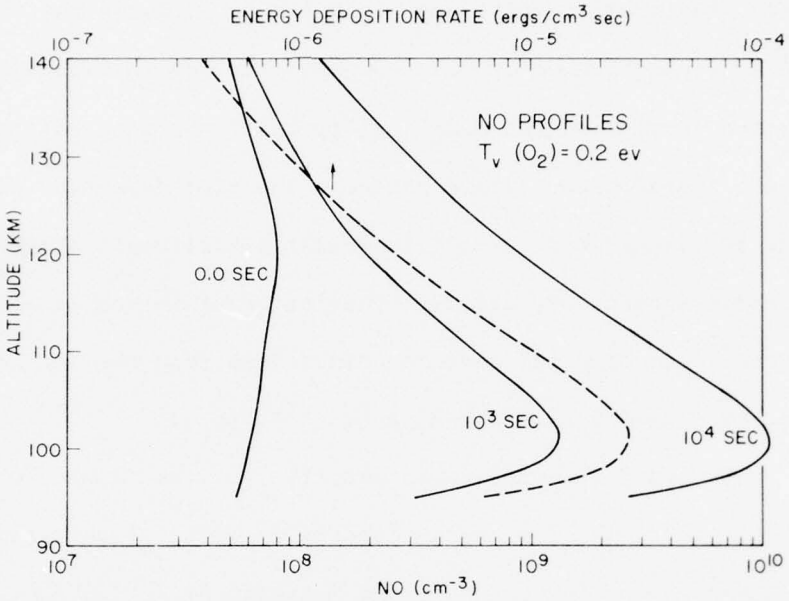

Fig. 4.2 — Altitude profiles of the [NO] buildup as a function of time for vibrationally hot O_2, $T_v(O_2)$ = 0.2 eV. The energy deposition rate is also illustrated and produces 26 kR of 3914 Å radiation at 100 km.

With 50% $N(^4S)$ production from $NO^+ + e$, the NO buildup is severely limited by the large chemical loss from the reaction $N(^4S) + NO$. However, such a large $N(^4S)$ production is not consistent with midlatitude data.[56,57] Our results are not sensitive to the selection of initial NO densities. The sensitivity of the NO buildup to a decreased O content of the model atmosphere is due to a reduction of odd nitrogen production, as more N_2^+ reacts with O_2 rather than with O. This reduction in NO production exceeds an opposite tendency due to reduced $N(^2D)$ quenching by O. An increase in the O content produces less pronounced [NO] changes.

4.3 CRITIQUE OF MODEL

The model can describe a rapid buildup of NO if the O_2 vibrational temperature, $T_v(O_2)$, is large, but the sources and sinks of O_2 vibrational energy must be compatible with high $T_v(O_2)$ in auroral arcs. Measurements at 1600-3300° K indicate that O atoms are efficient quenchers of O_2 vibrational energy.[62] Extrapolating their results down to 300° K, we obtain a quenching rate of $\sim 10^{-12}$ cm^3 sec^{-1} for $O_2(v=1)$. Two possible sources of O_2 vibrational excitation are the precipitating electrons and collisions of O_2 with translationally hot ions. In the former case less than 5% of the energy deposition is channeled into O_2 vibrational energy. Translationally hot ions, in particular O_2^+, may be able in collisions to efficiently excite $O_2(v)$. This latter process would be physically similar to Joule heating and maximum excitation would occur at ~ 125 km with negligible excitation below 110 km where the maximum [NO] enhancement

occurs [cf. reference 52 and Fig. 4.2]. The incorrect altitude variation and the observed ion composition preclude translationally hot ions as the source of $O_2(v)$. Whereas the precipitating electrons could excite O_2 in the appropriate altitude region, its source strength is not potent enough to overcome the severe quenching by O atoms to give high $T_v(O_2)$. High $T_v(O_2)$ is possible only if the O quenching rate were comparable to the slow O_2 and N_2 quenching rate at 300° K. We do note that Reid and Withbroe[63] suggest O_2 vibrational enhancement in the thermosphere from observations of solar UV radiation. A room temperature measurement of the O quenching rate would be decisive. On the basis of our present knowledge, it is unlikely that the O quenching rate is $\sim 10^{-18}$ cm^3 sec^{-1} at 300° K and hence high $T_v(O_2)$ is improbable in auroral arcs where large [NO] enhancements are inferred.

4.4 SPECULATIVE CHEMISTRY

In light of our previous discussion our search for potent auroral NO sources must become more desperate. In conventional chemistry approximately 10 eV of energy must be expended to initiate odd nitrogen production. The reaction $N_2 + O_2 \rightarrow 2NO$ is only endothermic by $\sim$ 2 eV and a potential factor of 10 increase in the NO production efficiency is possible. There is no experimental evidence to indicate that this reaction occurs even with vibrationally excited O_2 and/or N_2. But if it were possible to form NO by this reaction, there would be no chemical cutoff in the production of NO as present in the conventional chemical cycle.

The reaction $N_2 + O \rightarrow NO + N$ could also be considered with rate constant $\sim 10^{-10} \exp\left(\frac{-38000}{T}\right)$ cm^3 sec^{-1}. To compete with conventional NO sources, $K \sim 5 \times 10^{-19}$ cm^3 sec^{-1} or $T \sim 2000^0$ K. If N_2 were vibrationally hot and this energy were available to overcome the activation barrier, O atoms would quench $N_2(v)$ with a rate $\sim 3 \times 10^{-15}$ cm^3 sec^{-1},[64] much faster than the rate at which N and NO would be produced. The calculations of Schunk and Hays[65] support the conclusion that N_2 must have a Boltzmann distribution for vibrational energy in the E-region during auroral bombardment. Anharmonicity effects at higher vibrational levels would not negate their conclusions. Reaction $N_2 + O$ cannot be the source of anomalous auroral [NO].

4.5 DRIZZLE REGION

The available evidence suggests that the auroral zone undergoes continual bombardment by soft energetic electrons and only occasionally do spectacular events occur.[65] The continual bombardment of the auroral regions will lead to an enhanced background NO concentration. With the model, an attempt was made to estimate this concentration in the absence of transport for an electron deposition rate that produces 1 kR of the auroral green line (5577 Å), its threshold for detection. This deposition rate is equal to 0.03 of that in Fig. 4.2. A continual increase in the NO concentration with time is obtained until the NO cutoff density is reached at a time $\gg 10^6$ seconds. After 10^5 seconds, vertical transport effects will become important and severely limit the further NO buildup. However, peak NO

concentration $\sim 10^9$ cm^{-3} would be possible if the above electron deposition rate were constant with time. With such concentrations, the [NO] inferred by Donahue et al.[47] and Swider and Narcisi[48] from ion composition measurements would be possible without exotic chemistry, although it could not explain the peculiar kink in their deduced [NO] profile. In the case of the mass spectrometer measurements of large [NO] this source of NO fails by at least one order of magnitude.

4.6 CONCLUDING REMARKS

On the basis of our analysis we conclude that [NO] enhancements in excess of $0.1[O_2]$ are exceedingly improbable in auroral arcs. As a consequence, we are very skeptical of mass spectrometer measurements that exceed this limit. Any [NO] enhancement past this limit would be inconsistent with the chemistry discussed here with one exception, NO formation by $N_2 + O_2$. We emphasize that there is no experimental support for its occurrence. All other chemical schemes have the same difficulty; the NO buildup stops abruptly when [NO] reaches $\sim 0.1[O_2]$, because NO is not directly formed from N_2. The N_2 must be first dissociated; then, the N atoms are oxidized. A maximum NO buildup <u>rate</u> is achieved under these conditions only if the reaction $N(^4S) + O_2 \rightarrow NO + O$ is fast. The most plausible mechanism is vibrationally hot O_2 but limited data at shock tube temperatures suggest that O quenching is too severe to permit a departure from thermal equilibrium. A room temperature measurement of $O_2(v = 1) + O \rightarrow O_2(0) + O$ is desirable.

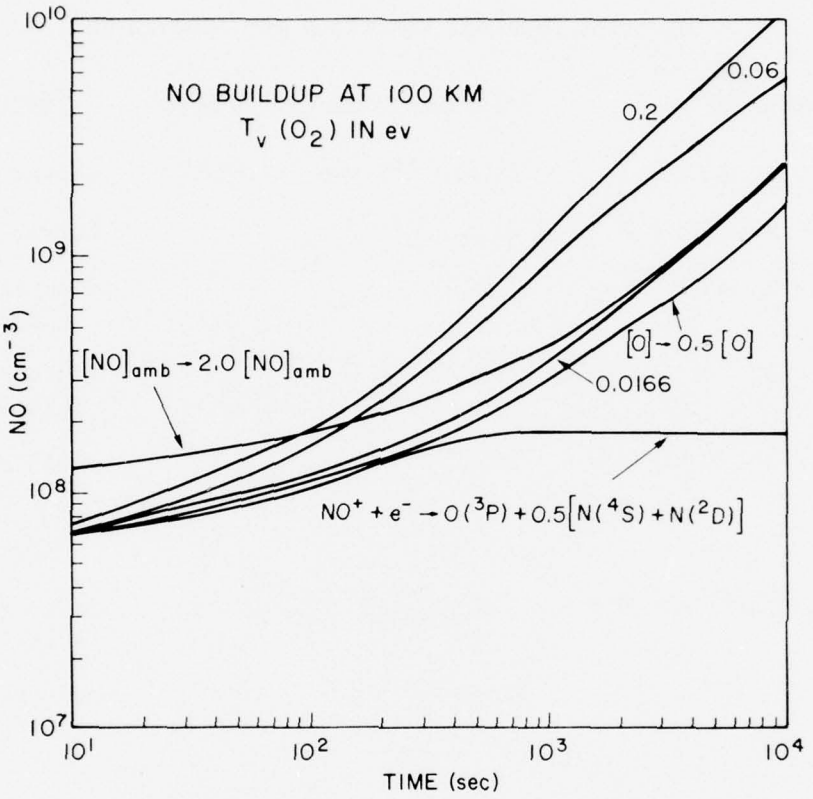

Fig. 4.3 — The [NO] buildup for various parameters as a function of time at 100 km where peak deposition occurs. For the standard run, denoted by 0.0166, only $N(^2D)$ is formed from $NO^+ + e$, $T_v(O_2)$ = 0.0166 eV = kinetic temperature, and [O] = 7×10^{10} cm^{-3} at 120 km. The label of the curve indicates the parameter varied. The labels, 0.2 and 0.6, denote the values of enhanced $T_v(O_2)$.

Table 4.1

Important Chemical Reactions for Auroral NO

Reaction	Rate Constant* (cm^3 sec^{-1})	Reference
$N(^4S) + O_2 \rightarrow NO + O$	$1.1 \times 10^{-14} T \exp(-3150/T)$	Garvin [1973]
$N(^4S) + NO \rightarrow N_2 + O$	2.7×10^{-11}	Garvin [1973]
$N(^2D) + O_2 \rightarrow NO + O$	7×10^{-12}	Slanger et al. [1971]
$N(^2D) + NO \rightarrow N_2 + O$	7×10^{-11}	Lin and Kaufman [1971]
$N(^2D) + O \rightarrow N(^4S) + O$	1×10^{-12}	Rusch et al. [1975] Strobel et al. [1975]
$N_2^+ + O \rightarrow NO^+ + N(^2D)$	$3.1 \times 10^{-8} T_i^{-0.44}$	McFarland et al. [1973]
$N_2^+ + O_2 \rightarrow O_2^+ + N_2$	$5.2 \times 10^{-8} T_i^{-0.8}$	McFarland et al. [1973]

*Temperatures in $^{\circ}K$

Section 5

EFFECTS OF ANOMALOUS RESISTIVITY ON AURORAL BIRKELAND CURRENT SYSTEMS

Joel A. Fedder

In recent years it has become widely recognized that geomagnetic field-aligned, Birkeland, electric currents are of considerable importance to the physics of the high-latitude ionosphere and magnetosphere. Although their existence in association with aurora was orginally proposed by Birkeland,[66,67] their importance only became evident as a result of the great number of measurements of magnetic field perturbations in the auroral regions by rockets and satellites. The rocket measurements[68-71] have shown clearly the association of Birkeland currents with auroral arcs and bands. Whereas, the satellite measurements[72-76] have shown that the field-aligned currents occur over a much wider region associated within the whole auroral oval.

The Birkeland currents in the auroral region arise from two different mechanisms. Energetic plasma pressure gradients in the magnetosphere can lead to field-aligned currents as discussed by Vasyliunas.[77] Additionally, the ionosphere can drive field-aligned currents caused by an imposed electric field in the presence of conductivity gradients or by an ionospheric conductivity in the presence of electric field gradients. These Birkeland currents couple the magnetospheric and ionospheric electric fields and to some extent must modify the spatial distribution and magnitude of each.[78]

Models for the field-aligned currents and electric fields have been developed for auroral arcs and for the auroral region as a

whole. Bostrom[79] presented a model for electric fields and current in arcs making two limiting assumptions concerning the magnitude of the Birkeland current. In one case the Birkeland current was allowed to flow freely while in the other, it was taken to be negligible. Atkinson[80] also presented a model for an auroral arc in which the return ionosphere electron current was strongly limited. In this paper results are presented which are similar to theirs. Models for the electric fields and currents in the auroral regions and lower latitudes as well have been developed by Wolf,[80] Jaggi and Wolf,[81] Iwasaki and Nishida,[82] Karlson,[83] and others. In most of this work the conductivity of the plasma along the geomagnetic field has been taken to be large, and therefore they show no effects of field-aligned resistance on the derived Birkeland currents and electric fields. One exception to this is the model of Coroniti and Kennel[84] for the polarization of the westward electrojet in the midnight auroral oval, caused by anomalous resistance to field-aligned current. However, the idea of anomalous resistance to field-aligned currents did not arise as a result of comparing model results to data for auroral electric fields and current, but rather, from a desire to explain the acceleration of auroral energetic particles.

Swift[85] proposed the existence of the ion acoustic instability in the auroral plasma which could lead to anomalous resistivity, a field-aligned electric potential, and the acceleration of auroral electrons. Subsequently, Kindel and Kennel[86] showed that for auroral plasma parameters, the ion cyclotron instability had a lower threshold and therefore would be a more likely mechanism for the

anomalous resistivity. Furthermore, the threshold for this current driven instability is well within the range of Birkeland current densities inferred from measurements. A further study of the ion cyclotron instability by Palmadesso et al.[87] demonstrates the self-quenching character of the instability which results in marginal instability and considerably lower resistivity. In addition to the current driven plasma instabilities mentioned above Papadopoulos and Coffey[88,89] have proposed a beam driven parametric instability which also may provide resistance to auroral Birkeland currents. In this mechanism, a precipitating electron beam drives high-frequency plasma waves which interact parametrically to drive lower frequency waves and plasma density fluctuations. This parametric instability has the virtue that in addition to providing anomalous resistivity, it also stabilizes the beam plasma interaction and enhances the tail density in the thermal electron distribution to agree with auroral particle measurements.[90]

Mechanisms other than plasma instabilities and anomalous resistance have been suggested which could lead to field-aligned electric potentials. It would be expected that these mechanisms also would greatly affect Birkeland current systems. One of these is the possible formation of electrostatic double layers[91,92] which could lead to a large potential drop over a small distance along the magnetic field. The other is the possible formation of electrostatic shock waves between the magnetosphere and ionosphere. Kan[93] has discussed normal electrostatic shocks while Swift[94] has discussed the possible occurrence of oblique electrostatic shocks and their effects on

particles and electric fields.

In this section we attempt to discuss in considerable detail the effects of anomalous resistance on auroral Birkeland currents. We will illustrate and delineate these effects by showing a rather large selection of results from numerical model studies. In the following section the important features of the auroral model are presented. We also will present a simple model for the ionosphere-magnetosphere interaction with anomalous resistivity to field-aligned currents.

The section on results will demonstrate the effects of anomalous resistivity on Birkeland currents. Results are presented for both the minimum and maximum magnitude of resistivity which can reasonably be expected. Also to be presented are model results for the two most likely resistive mechanisms. We show the effect of treating the precipitating current separately from the ionospheric electron Birkeland current. These results are discussed and some conclusions will be drawn.

Since the simple model used to show the effects of anomalous resistivity is probably not very realistic for comparison to real auroral arcs, in the final section we will present and discuss the results of one model for the midnight region of the auroral oval. The complex current systems in this model will be discussed in some detail. We will also demonstrate that the electric fields derived from this model are in agreement with satellite electric field measurements.

5.1 MATHEMATICAL MODEL

To describe the auroral ionosphere, we solve the plasma continuity equation

$$\frac{\partial n}{\partial t} + \nabla_{\perp} \cdot (n\underline{v}_{\perp}) = P - \alpha n^2 \ , \tag{5.1}$$

the plasma momentum equation

$$\frac{q}{m} (\underline{E}_{\perp} + \frac{1}{c} \underline{v}_{\perp} \times \underline{B}) = \nu \underline{v}_{\perp} \ , \tag{5.2}$$

and the current continuity equation

$$\nabla \cdot \underline{j} = 0 \ . \tag{5.3}$$

In Eq. (5.1) we have neglected vertical transport of the plasma; in Eq. (5.2), the inertial terms; and in Eq. (5.3), charging effects. In Eq. (5.1), n, $\underline{v}$, P, and α are respectively the plasma density, the ion velocity, the plasma volume production rate, and the volume dissociative recombination rate; and the symbol $\perp$ applies to the geomagnetic field. The symbols in Eq. (5.2), q, m, E, c, B, and ν are respectively the electron or ion charge, and electric field in the ionosphere, the speed of light, the geomagnetic field and the electron- or ion-neutral collision frequency. The current density, in Eq. (5.3), is defined by

$$\underline{j} = en(\underline{v}_e - \underline{v}_i) \ , \tag{5.4}$$

where e is the electron charge and $\underline{v}_e$ and $\underline{v}_i$ are the electron and ion velocities.

These equations are solved on a cartesian coordinate system with the x-axis directed north-south; the y-axis, east-west; and the z-axis, vertical. In this paper, for simplicity, it is assumed that

all ionospheric properties are constant along the y-dimension. Additionally, the geomagnetic field is taken to be directed along negative z. Although these assumptions are not necessary to achieve a valid solution, they do make the results much easier to interpret.

In order to complete the set of Eqs. (5.1 - 5.4), it is necessary to prescribe the electric field. We define $\underline{E}$ in terms of the electric potential,

$$\underline{E} = \nabla \psi^{I} \quad , \tag{5.5}$$

which is defined by the magnetosphere-ionosphere interaction, Ohms Law;

$$\psi^{I} = \psi^{M} + J_{||} R \quad . \tag{5.6}$$

ψ_I is the ionospheric electric potential, ψ_M the prescribed magnetospheric potential on the same field line. $J_{||}$ is the field-aligned current leaving or entering the top of the horizontally conducting ionosphere (200 km altitude), and R is the resistivity integrated along a field line from 200 km altitude to the equatorial plane in the magnetosphere. Eq. (5.6) implies that the magnetosphere is an intrinsic source of electric potential which drives the ionosphere and Birkeland current systems. Although taking the auroral magnetosphere as a source of either electric field or current is not usual (see discussion by Wolf[78]), other workers have made such an assumption.[95,96]

Eqs. (5.1) - (5.6) are a complete set and may be solved self-consistently to yield the plasma density, electric field, and current system provided that P (in Eq. (5.1)) and ψ_M and R (in Eq. (5.6)) are specified. The production rate, P, was chosen to

closely resemble the 3914 Å emission data of Romick and Belon.[97] Using typical values for the recombination rate and the collision frequencies,[98] the maximum Pedersen conductivity in the auroral arc is enhanced a factor of 5.2 over that outside, and the Hall to Pedersen conductivity ratio is 2.4. We judge that these values are typical of many auroral arcs. ψ_M is chosen to yield an electric field perpendicular to the arc, in the x direction, which has a strength of 25 millivolts per meter. This is the simplest situation for the electric field about an auroral arc, and therefore allows us to more clearly show the effects of the resistance on the Birkeland current. The resistance function has been chosen differently for each result and will be described with the results.

To obtain a self-consistent result, it is necessary to obtain a simultaneous solution of (5.1) - (5.6). The results presented here were obtained as follows:

a. Using assumed ψ_M , obtain $\underline{E}$ from (5.6) and (5.5) with $J_{||}(t = 0) = 0$,

b. Obtain $\underline{v}$ from (5.2),

c. Advance n in time with (5.1),

d. Obtain $J_{||}$ using (5.3 and (5.4),

e. Compute $\underline{E}$ from (5.6) and (5.5),

f. Repeat b - e until a steady state is achieved.

The equations are solved for the altitude range, 95 - 200 km, where the perpendicular ionospheric currents occur. The results include n and $\underline{j}$ throughout this region, and ψ_I and $J_{||}$ at 200 km altitude.

5.2 RESULTS

In this section the effects of anomalous resistivity on auroral Birkeland currents are explored by consideration of a group of examples. We first consider the effect of the magnitude of the resistivity on the amplitude of the Birkeland current density and on the electric field perturbation. We next consider the results of anomalous resistivity for two of the proposed plasma mechanisms; the current driven ion cyclotron instability and the beam driven parametric instability. Finally, results are shown for a number of cases in which the precipitating current is resistance free and only the return currents experience resistivity.

Figure 5.1 shows the result for the minimum amount of resistivity that can be expected along an auroral field line. The resistance was chosen at a constant value of 3.5×10^{-4} e.s.u. This value is the Spitzer[99] resistance of a 1 cm^2 flux tube above 200 km at auroral latitudes. The Birkeland currents peak strongly at the edges of the arc while the electric field perturbation is negligible. The maximum current density has the value 5.4×10^{10} el cm^{-2} sec^{-1} (8.65×10^{-5} amp m^{-2}) which is considerably larger than current densities normally observed. This result is quite similar to one originally discussed by Bostrom.[79]

Figure 5.2 shows a contrasting result to Figure 5.1. In this case the resistance is again constant but now is the maximum value that can reasonably be expected along auroral field lines. Its value is 2×10^4 larger than the Spitzer value and is comparable to that used in previous work by Coroniti and Kennel.[84] For such a large value of

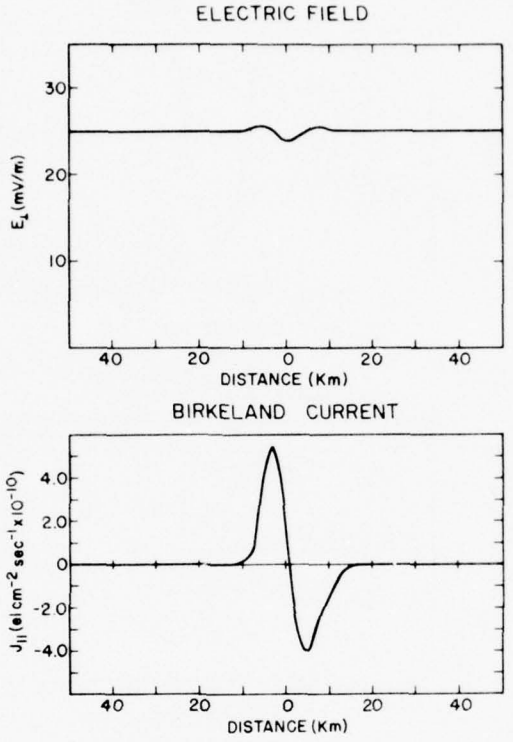

Fig. 5.1 — Electric field and Birkeland current density for a very small resistance to field-aligned current. The resistance, R = 0.00035 esu, (the Spitzer resistance of a 1 cm^2 flux-tube above 200 km altitude) is spatially constant. For this small resistance the electric field perturbation is small in the auroral arc while the Birkeland current density is very large, up to 8.65×10^{-5} amp m^{-2}.

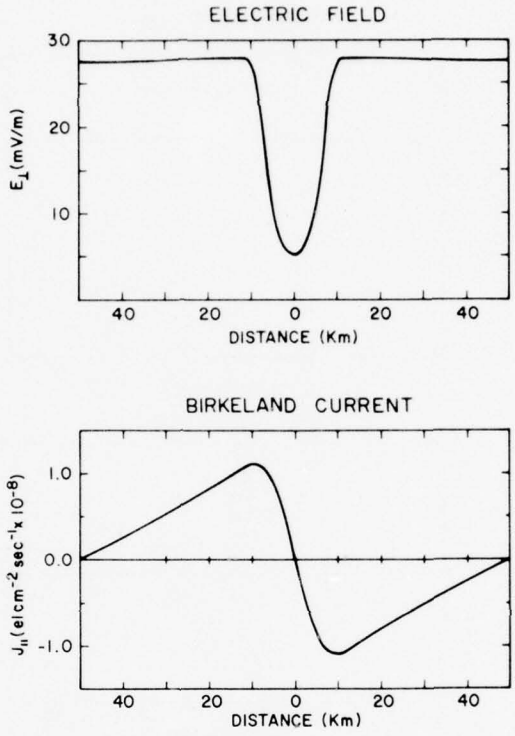

Fig. 5.2 — Electric field and Birkeland current density for a very large resistance. The resistance, 7 esu, is spatially constant and a factor of 2×10^4 larger than the Spitzer value. For this large resistance the Birkeland current density is 500 times smaller than in the previous case. Whereas, the electric field is greatly reduced inside the auroral arc.

resistance, the results show that the Birkeland current is small 1.1×10^{8} el cm^{-2} sec^{-1} (1.76×10^{-7} amp m^{-2}) and that the electric field is greatly reduced in the auroral arc. The Birkeland current density is smaller than what is normally observed whereas the electric field strength is anti-correlated with the arc as has been observed.[100] As in the previous case, this type of situation has also been discussed by Bostrom.[79]

The results in Figure 5.3 are intermediate between those shown in the first two figures. In this case the resistance has the constant value 0.3 esu. The electric field and Birkeland current patterns are quite similar to those of the previous case. But here, the current density has a maximum of 4×10^{-6} amp m^{-2}, which is more typical of measured values. In all of these cases where a constant resistance was chosen, the Birkeland currents maximize at the strong density gradients on this side of the auroral arc. On the other hand, the electric field shows a minimum in the center of the arc and tends to have maxima outside the arc structure.

For the next result, we attempt to model a marginally unstable current driven resistance mechanism. Marginal instability is a reasonable condition as the current driven instabilities are self-saturating. The marginal instability model assumes that the resistance on each flux tube is incrementally increased above the Spitzer value at each time step when the Birkeland current density exceeds a threshold of 3×10^{9} el cm^{-2} sec^{-1}.[84] The result is shown in Figure 5.4. The electric field is quite similar to that in the previous case, however, the Birkeland current is considerably different. The Birkeland current

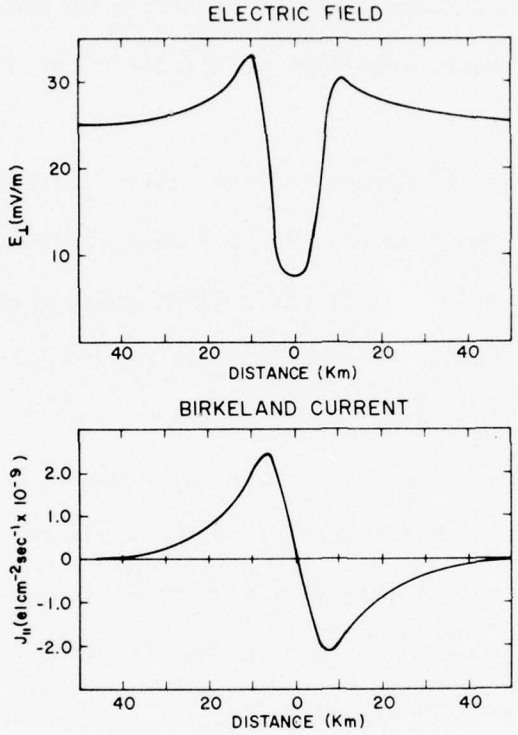

Fig. 5.3 — Electric field and Birkeland current density for an intermediate value of resistance. The resistance is spatially uniform and has a value of 0.28 esu. The Birkeland current density has a reasonable magnitude, about 4×10^{-6} amp m^{-2}. The electric field is enhanced outside the auroral arc and considerably reduced inside.

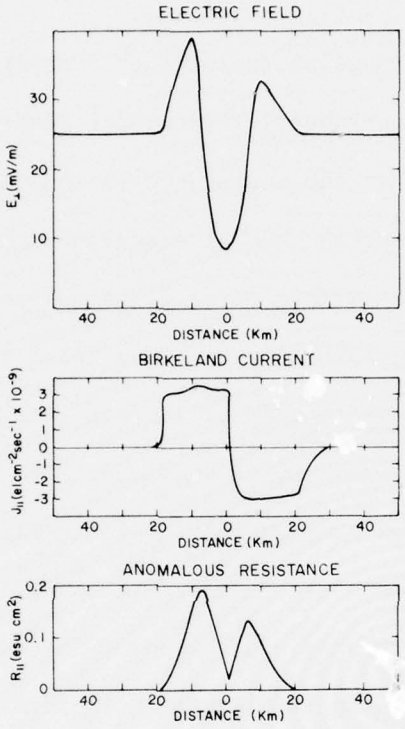

Fig. 5.4 — Electric field, Birkeland current density and anomalous resistance of 1 cm^2 flux tube for the current driven anomalous resistance mechanism. The resistance is uniform at the Spitzer value except where the current exceeds the instability threshold of 4.8×10^{-6} amp m^{-2}, in which case the resistance increases rapidly. The Birkeland current density has a square wave character with the amplitude of the instability current threshold. The electric field is quite similar to that in Fig. 5.3.

has the shape of a square wave to either side of the center of the arc. The resistance of a 1 cm^2 flux tube is also shown. We see that it peaks at the steep density gradients on either side of the arc, and has a maximum value which is about 500 times larger than the Spitzer resistivity.

Figure 5.5 shows the results of a preliminary attempt to model the beam driven parametric resistance mechanism. Papadopoulos and Coffey[88] showed that the resistance is roughly proportional to the energy in the precipitating beam of electrons. Here we assume, similarly, that the resistance is proportional to the total ionization production rate in the auroral arc. This leads to a resistance which is large, 0.3 esu, at the center of the arc but has the Spitzer value immediately outside. The results show that both the Birkeland current and electric field peak very sharply in the small resistance region immediately outside the arc. To the author's knowledge, such strong peaking has not been observed in the auroral data.

In the preceding results both precipitating and cold ionospheric particle currents where treated identically. In all these cases the Birkeland current was balanced across the center of the auroral arc density enhancement and there was no evidence of an energetic precipitating current. The next three samples will show results in which the effect of the precipitating particles is clearly seen. In these cases it is assumed that only the cold, ionospheric particle return currents experience anomalous resistance. The precipitating particles carry current resistance-free.

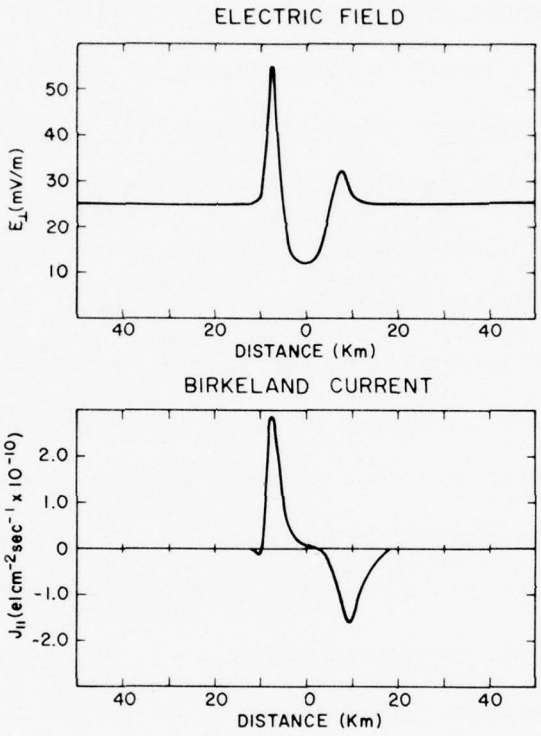

Fig. 5.5 — Electric field and Birkeland current density for the beam driven, parametric resistance mechanism. Here the resistance has the Spitzer value outside the auroral arc, but is very large and proportional to the precipitating energy inside. The Birkeland current density is small inside the arc but becomes large at the edges. The electric field is also very large at the border of the arc.

Figure 5.6 shows one of these results in which the resistance is large, 7 esu, but localized to the auroral arc field lines. In this case the precipitating particle current (short dash line) carries almost all of the Birkeland current inside the arc. The ionospheric electron return current exists outside the arc in a region of low resistance. These results are, likely, a better model for the beam driven parametric resistance mechanism than those of Figure 5.5.

Figure 5.7 shows a similar result but in this case the resistance is smaller, 0.3 esu, and is constant. Here, the precipitating current is shown by the short dash line, the cold, ionospheric return current, by the long dash line, and the net Birkeland current, by the solid line. Again, the effect of the precipitating particles is clearly evident in the total Birkeland current density. Nevertheless, the ionospheric return current is substantial inside the auroral arc and reduces the current density in that region. This effect becomes even more apparent in the results of Figure 5.8. For this result, the constant resistance was reduced a factor of 5 from that in Figure 5.7. The net Birkeland current density in Figure 5.8 no longer shows an extrema in the region of the arc precipitation and is, here again, balanced across the center of the auroral arc. Any further reduction in the anomalous resistance would lead to almost complete cancellation of the precipitating particle current by the cold, ionospheric return current.

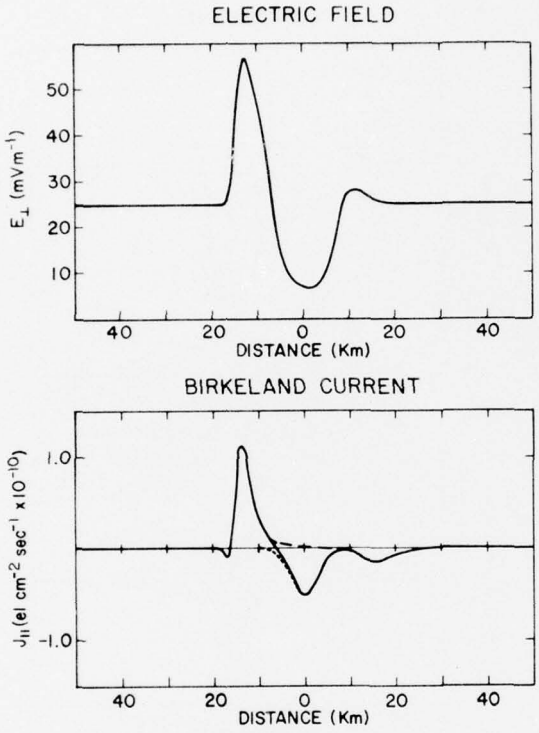

Fig. 5.6 — Electric field and Birkeland current density for resistance free precipitating particle current. The resistance to the ionospheric return current has the Spitzer value outside the auroral arc and is very large inside. The short-dash curve shows the precipitating current; the long-dash curve shows the ionospheric return current; and the solid line is the net current density. The precipitating energetic particles carry almost all of the electron current into the ionosphere. The return currents are strong in the Spitzer resistance region outside the auroral arc. This is likely a better result for the beam driven resistance mechanism than shown in Fig. 5.5.

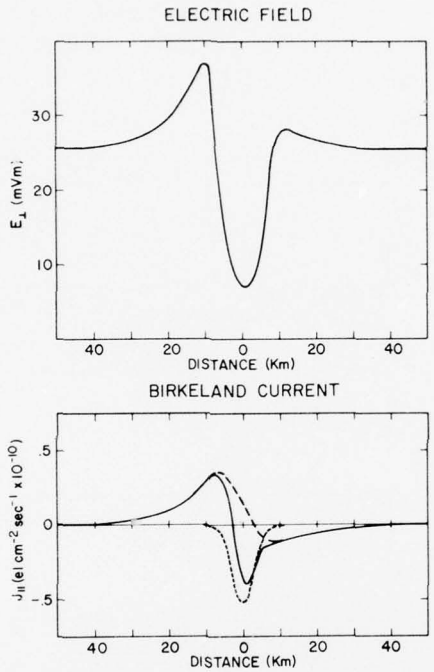

Fig. 5.7 — Electric field and Birkeland current density for a similar case to Fig. 5.6. Here the resistance is spatially uniform and has a moderate value, 0.3 esu. The presence of the resistance free precipitating current (short-dash curve) is evident in the net Birkeland current density (solid curve), however, it does not account for more than about half of the net downward electron flow. The electric field is similar to that in Figs. 5.3 and 5.4.

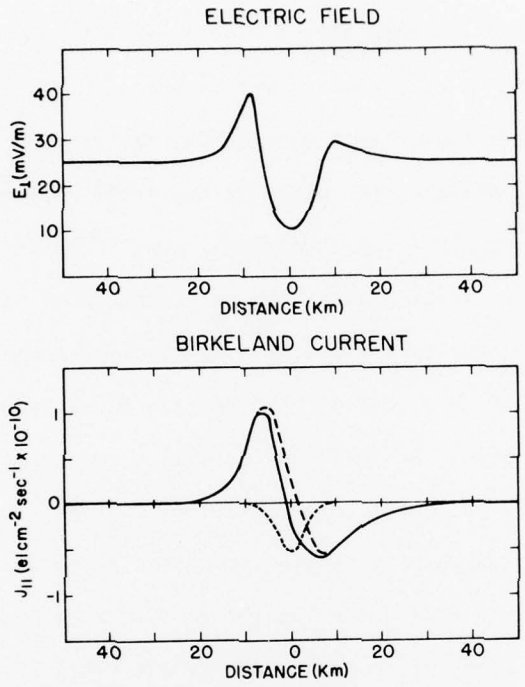

Fig. 5.8 — Results for the same conditions as in Fig. 5.7 except that the resistance is reduced a factor of 5. The contribution of the precipitating current to the net Birkeland current density is now much less obvious. The spatial distribution of the Birkeland current is similar to that in the first 3 figures. Further reduction of the anomalous resistance would lead to a result like Fig. 5.1.

5.3 DISCUSSION

In the preceding section a large number of examples were presented of the possible effects of anomalous resistivity by an auroral Birkeland current. The problem which remains is to sort out the effects and to develop some idea of their possible importance and relevance. That, we will now attempt to do.

We think that, taken as a whole, the results presented here are not in great disagreement with the available data on auroral Birkeland currents and electric fields. That is to say, using a model similar to that presented here which makes reasonable assumptions concerning the magnetospheric electric field and the anomalous resistivity mechanism can lead to a good fit between the model results and the auroral measurements. We therefore feel that there is some validity in applying the model results to the auroral currents and resistivity.

The model results indicate that the anomalous resistivity on auroral field lines is a factor of 10^2 to 2×10^4 greater than the Spitzer value. There are a number of reasons for this. If the resistivity is too small, the Birkeland current density can easily exceed the observed range of the measurements, $1 - 20 \times 10^{-6}$ amp m^{-2}. Moreover, as was seen in the results of Figure 5.8, a small resistance allows the ionospheric return current to almost completely neutralize the precipitating electron current. The upper value of the resistivity is set by plasma instability considerations and has been discussed elsewhere.[88]

In addition, the model results would favor a resistivity which varies slowly in space. Rapid changes in the resistance of

adjacent flux tubes leads to sharp extrema in both the Birkeland currents and in the electric field. Spatial changes in the resistance are important, however, as they greatly influence the spatial distribution of the Birkeland current density. This is particularly well shown in the contrasting results of Figures 5.4 and 5.5. The effect of a spatially non-constant resistance is to alter the electric field so that the Birkeland current is stronger in regions of lower resistivity and weaker in regions of higher resistivity.

Finally, we would make an observation regarding the acceleration of auroral particles by geomagnetic field-aligned potential drops which are created by anomalous resistivity. For the results shown here, the largest field-aligned potential drop is 110 volts. Even if the magnetospheric electric field were 10 times stronger, it could not explain the energization of auroral electrons to more than 1 kilovolt. This does not mean that the mechanism does not occur, but only that it cannot occur on the scale size ($\sim$ 10 km) of a single auroral arc. In fact we will see an indication that it does occur in a more realistic model of auroral arcs which follows.

5.4 RESULTS FOR A MORE REALISTIC MODEL

The results shown and discussed in the previous sections were derived from a very simple model of an auroral arc and therefore would not be expected to describe accurately the fields and currents in an actual aurora. The simple model was used in order to show more clearly the effects of anomalous resistance on auroral Birkeland currents. Here we will attempt to show that anomalous resistivity is important in

the auroral oval by use of a more realistic model. This model was devised in an attempt to understand and explain the OGO-6 electric field measurements from the midnight region of the auroral oval presented by Maynard.[101]

The model requires the assumption of the magnetospheric electric field and energetic particle precipitation pattern along a north-south meridian through the premidnight auroral oval. The northward electric field chosen is 16 millivolts/meter, constant across the oval; and no northward field outside of the oval. The westward electric field is taken to be 25 millivolts/meter north of the oval, decreasing linearly to zero from the northern to southern border of the oval, and zero in the region south of the auroral oval. This choice for the magnetospheric electric field is somewhat unconventional and controversial, however it is in agreement, we think, with the flow pattern proposed for the plasma sheet by Rostoker and Bostrom[95] for the immediate premidnight region.

The precipitation pattern chosen, is shown as the short dash line in Figure 5.9. It features a broad (400 km wide) precipitation region in the southern and central regions of the oval and a structured region (containing 2 arcs or bands) at the northern border of the auroral oval. We would interpret the broad region as plasma sheet particle precipitation and the structured region as inverted - V precipitation. The precipitation pattern has been designed to be similar to the Ariel 4 particle data of Craven and Frank.[102]

Figure 5.9 also presents the resulting field aligned current systems when a uniform, large (7 esu) anomalous resistance is assumed.

The solid line shows the net field-aligned current density, the long dash line shows the cold ionospheric electron current, and the short dash line shows the precipitating current. The direction and strength of the net current is consistent with the TRIAD satellite date.[103] The important effect of the anomalous resistance is to cause the hot and cold particle currents to oppose each other in the broad precipitation region and to have the same direction in the structured precipitation region. Rocket magnetometer data have been interpreted to indicate that both hot and cold electrons flow downward into arcs [see Anderson and Cloutier[104] and references therein].

In addition to the cold ionospheric current the long dash line in Figure 5.9 is a plot of the field-aligned potential difference. The units in this case are kilovolts. In the structured region the potential is directed upward and becomes as large as 2 kilovolts. Presumably this potential could serve to accelerate electrons into the ionosphere. In the broad precipitation region the potential is downward and thus would discourage electron precipitation and encourage ion precipitation.

Figure 5.10 is a comparison between a measured electric field[101] and the model electric field result. The antenna for the measurement was oriented north-east south-west and therefore the model field was plotted on the same axis. In each case the major features of the field are the same. At the southern border the field is northward; it passes through zero at the Harang Discontinuity (Maynard's identification) and becomes northward through the central region of the auroral oval. At the northern border, both fields oscillate rapidly before

turning basically westward in the polar region. The agreement between the model electric field and the measurement is good.

In this paper we have shown that a model incorporating anomalous resistivity to field aligned currents can provide a description of auroral electric fields and currents, which is in reasonable agreement with auroral measurements. It was also shown that the effects of the resistivity were important to the Birkeland current densities derived therefrom. A better evaluation of resistivity and its effect on auroral fields and currents can be made only by incorporating the actual plasma mechanisms and their nonlinear behavior in the auroral model.

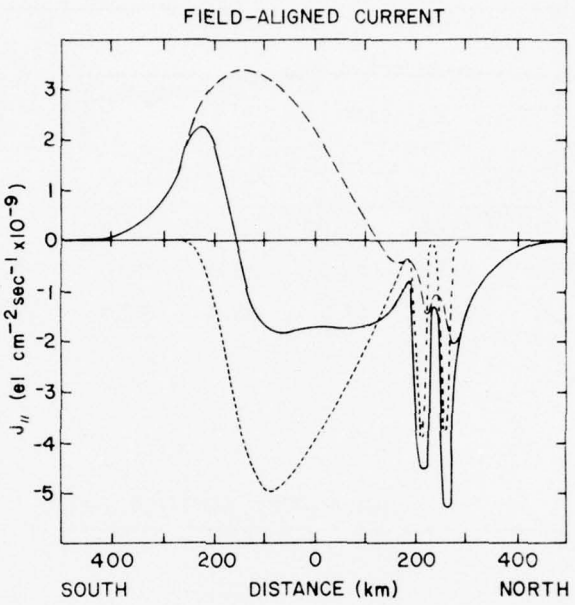

Fig. 5.9 — The field-aligned current density for a more realistic model of auroral arcs in the premidnight auroral oval. The short-dash curve shows the precipitating energetic electron current. It is composed of a broad precipitation region (plasma sheet particles) in the southern and central part of the oval, and two discrete, narrow precipitation structures (auroral arcs or bands) at the northern border of the oval. The long-dash curve shows the cold-ionospheric electron current. In the southern and central portions of the oval the hot and cold particle currents oppose each other, while at the northern border they are in the same direction. The solid curve shows the net field-aligned current density which results. In addition to the cold ionospheric current, the long-dash curve shows the potential drop along the geomagnetic field; the appropriate units are kilovolts. The potential is upward and accelerates precipitating electrons into the discrete precipitation region, while opposing electron precipitation in the broad region.

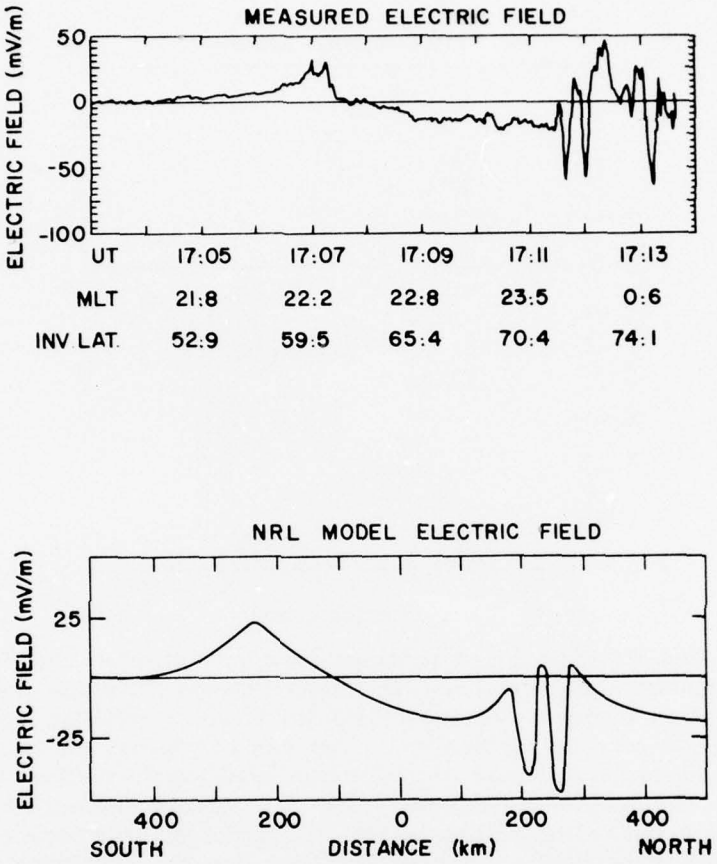

Fig. 5.10 — A comparison between a measured electric field [Maynard, 1974] and the model electric field for the currents of Fig. 5.9. Both the measured and model fields have the same features. The field is northward at the southern border of the auroral oval, becomes southwestward through the central oval, and shows similar structure in the discrete precipitation region at the northern border.

Section 6

SUMMARY

In the introduction, we have pointed out the considerable similarities between the effects of a HANE and those of an auroral disturbance. These similarities include precipitation of energetic particles, generation of field-aligned current systems, atmospheric heating and generation of winds, radiation throughout the electromagnetic spectrum, along with other plasma phenomena. One result of these various processes is the creation of communications disturbances and interruptions which can be far reaching and of long duration. It is the study of these phenomena and their resulting effect on communications systems which is the motivation for the work reported here.

This is not to say that the aurora demonstrates these nuclear phenomena in the same magnitude and to the same extent as a HANE, but rather that the same physical laws and, therefore, similar models describe the effects in both events. The aurora can therefore be used, in the absence of nuclear testing, as a benchmark for nuclear phenomenology. Moreover, the physical models developed in the auroral program can be applied, with some modification, to the study of nuclear phenomenology. The auroral program, in this manner, is an integral part of the study of HANE effects on communication systems.

A program for developing an auroral model must address three fundamental technical areas: 1) the deposition of energy in the upper atmosphere by energetic electrons and protons 2) the chemical reactions initiated by the deposited energy and 3) the electrodynamical aspects

such as the structures of fields and currents. This program closely parallels the approach necessary in modeling HANE effects and provides valuable insights for the understanding of HANE phenomenology as well as serving as a measuring standard for our ability to model perturbations (or HANEs) in the upper atmosphere.

During the past year, significant improvements have been incorporated into the NRL proton deposition model. The number of atmospheric constituents in the model has been increased with the addition of O and O_2 to the N_2 already in the program. The photon energy degradation treatment, based on the continuous slowing down approximation, has been improved by the inclusion of the influence of the geomagnetic field on the particle energy loss.

Progress has also been made in electron energy deposition. The NRL electron transport code has predicted higher backscatter than other models because of the way the energy loss process is treated. A detailed study reveals high sensitivity of the backscattered flux to variations in the large angle scattering cross sections. The numerical solutions to the equation of transfer are shown to be accurate to at least three significant figures.

Auroral chemistry studies were focused on the large enhancements of NO concentration in auroral arcs inferred from observations. An analysis in terms of a model incorporating the possible channels of NO buildup has indicated that NO enhancements in excess of 10% of the concentration of O_2 would be improbable.

Improvements have been made in the auroral electrodynamics models. A detailed assessment of the importance of anomalous plasma

resistivity in modeling auroral electric fields and currents has been made. These model results have been shown to be in good agreement with auroral measurements.

The studies above have all contributed to other areas of the nuclear effects program. For instance, the proton energy deposition method has been modified to describe the deposition of nuclear debris ions and has given results which compare well with data from bomb test programs. It is now used as an important part of HANE simulations. Changes have also been made in HANE chemistry codes as a direct result of auroral chemistry studies. The auroral electrodynamics studies and models show promise of making important contributions in the near future as nuclear phenomenology studies are carried to later times. Much of the theoretical developments in the auroral models are directly applicable to the electrostatic evolution of the nuclear debris and ionized plasma which is of great importance in evaluating very late time effects of HANEs on defense satellite communications systems.

Future work will be devoted to studying the occurrence and development of plasma irregularities in the auroral ionosphere. The electrodynamic models used for this study are closely related to the late-time electrostatic models of HANEs. It is expected that these studies will allow a direct connection to be made between scintillations at auroral latitudes observed in the Wideband Satellite Experiment and those which would occur in the nuclear environment. The auroral modeling program is unique in allowing a direct connection to be made between naturally occurring scintillations and HANE effects on communications.

In conclusion, we point out that the auroral modeling program has made direct, important contributions to HANE phenomenology studies. Moreover, it is expected that such benefits will continue to accrue. As interest increases in nuclear disturbance effects at later times, the auroral modeling effort and the electrostatic methods and techniques developed through it will become a foundation of future developments in HANE phenomenology. In addition it will allow a connection to be made between nuclear weapons effects on communications and measurements which are conducted in the natural environment.

ACKNOWLEDGEMENT

The authors would like to acknowledge the many helpful suggestions and information received from other staff members and, particularly, the assistance of Dr. T. P. Coffey. They would also like to thank Dr. J. Block for assembling this report.

AD-A043 259 NAVAL RESEARCH LAB WASHINGTON D C F/G 4/1
NUMERICAL MODELING OF AURORA VOLUME I OF THE CALENDAR YEAR 1975--ETC(U)
APR 77

UNCLASSIFIED NRL-MR-3462 NL

2 OF 2
AD
A043259

END
DATE
FILMED
9-77
DDC

REFERENCES

1. A. E. S. Green and C. A. Barth, J. Geophys. Res. 70, 1083 (1965).
2. R. S. Stolarski and A. E. S. Green, J. Geophys. Res. 72, 3967 (1967).
3. P. M. Banks, C. R. Chappell and A. F. Nagy, J. Geophys. Res. 79, 1459 (1974).
4. M. J. Berger, S. M. Seltzer and K. Maeda, J. Atmos. Terr. Phys. 32, 1015 (1970).
5. M. Walt, W. M. McDonald and W. E. Francis, "Penetration of Auroral Electrons into the Atmosphere" in Physics of the Magnetosphere, ed. R. L. Carovillano, D. Reidel, Dordrecht, Netherlands (1969).
6. D. J. Strickland and P. C. Kepple, "Preliminary Report on the Transport and Production of Energetic Electrons in Auroras," NRL Memorandum Report 2779 (1974).
7. A. Dalgarno, M. B. McElroy and A. I. Stewart, J. Atmos. Sci. 26, 753 (1969).
8. P. S. Julienne, "A Continuous Slowing-Down Electron Energy Deposition Model," NRL Memorandum Report 2958 (1974).
9. R. H. Eather and K. M. Burrows, Aust. J. Phys. 19, 309 (1966).
10. R. H. Eather, Ann. de Geophys. 2, 609 (1970).
11. R. H. Eather, Rev. of Geophys. 5, 207 (1967).
12. A. B. Prag, F. A. Morse and R. J. McNeal, J. Geophys. Res. 71, 3141 (1966).
13. G. T. Davidson, J. Geophys. Res. 70, 1061 (1965).
14. B. C. Edgar, W. T. Miles and A. E. S. Green, J. Geophys. Res. 78, 6595 (1973).

15. J. E. Rogerson and J. Davis, Preliminary Report on a Program to Study Proton Deposition in the Atmosphere, NRL Memorandum Report 2967, (1975).

16. R. C. Wentworth, W. M. McDonald, and S. F. Singer, Phys. Fluids 2, 499 (1959).

17. G. W. Prölss, Planet. Space Sci. 21, 1681 (1973).

18. S. K. Allison, Rev. Mod. Phys. 30, 1137 (1958).

19. A. E. S. Green and L. R. Peterson, J. Geophys. Res., Space Phys. 73, 233 (1968).

20. R. J. McNeal and J. H. Birely, "Basic Processes and Cross Sections in Proton Auroras," The Radiating Atmosphere (B. M. McCormac, ed.), D. Reidel Pub. Co., Dordrecht, Holland (1971).

21. R. J. McNeal and J. H. Birely, Rev. Geophys. Space Phys. 11, 633 (1973).

22. R. F. Stebbings, A. C. H. Smith and H. Ehrhardt, J. Geophys. Res. 69, 2349 (1964).

23. R. H. Neynaber, J. A. Rutherford, and D. A. Vroom, New Atomic Bean Studies at Low Energies, INTEL-RT 8100-005 (DNA 3384F) (20 August 1974).

24. L. G. Jacchia, "Static Diffusion Models of the Upper Atmosphere with Empirical Temperature Profiles," Smithsonian Inst. Astrophys. Observ., Cambridge, Mass., Smithsonian Special Report 1965.

25. J. W. Chamberlin, Physics of the Aurora and Airglow, Academic Press New York (1961).

26. D. Rapp, P. Englander-Golden, J. Chem. Phys. 43, 1464 (1965).

27. B. L. Schram, F. J. de Heer, M. J. Van der Wiel, J. Kistemaker, Physics 31, 94 (1965).

28. W. L. Borst, Phys. Rev. A5, 648 (1972).

29. P. N. Stanton, R. M. St. John, J. Opt. Soc. Am. 59, 252 (1969).

30. S. Chung, C. C. Lin, Phys. Rev. A6, 988 (1972).

31. T. G. Finn, J. F. M. Aarts, J. P. Doering, J. Chem. Phys. 56, 5632 (1972).

32. J. F. M. Aarts, F. J. de Heer, Chem. Phys. Lett. 4, 116 (1969).

33. A. Chutjian, D. C. Cartwright, S. Trajmar, Phys. Rev. Letters 30, 195 (1973).

34. A. E. S. Green, R. S. Stolarski, J. Atmos. Terr. Phys. 34, 1703 (1972).

35. G. J. Schulz, Phys. Rev. 135, A988 (1964).

36. D. Spence, J. L. Mauer, G. J. Schulz, J. Chem. Phys. 57, 5516 (1972).

37. F. Linder, A. Schmidt, Z. Naturforsch, 26a, 1617 (1971).

38. S. Trajmar, D. C. Cartwright, W. Williams, Phys. Rev. A4, 1482 (1971).

39. S. Trajmar, W. Williams, A. Kuppermann, J. Chem. Phys. 56, 3759 (1971).

40. W. L. Fite, R. T. Brackmann, Phys. Rev. 113, 815 (1959).

41. R. J. W. Henry, P. G. Burke, A. L. Sinfailam, Phys. Rev. 178, 218 (1969).

42. E. Zipf (private communication).

43. D. J. Strickland, D. L. Book, T. P. Coffey, and J. A. Fedder, submitted to J. Geophys. Res. (July 1975).

44. J. H. Jacob, Phys. Rev. A8, 226 (1973).

45. H. A. Bethe, M. E. Rose, and L. P. Smith, Proc. Am. Phil. Soc. 78, 573 (1938).

46. M. N. Rosenbluth, W. M. MacDonald and D. L. Judd, Phys. Rev. 107, 1 (1957).

47. T. M. Donahue, Radio Sci. 7, 73 (1972).

48. W. Swider and R. S. Narcisi, Planet. Space Sci. 18, 379 (1970).

49. W. Swider and R. S. Narcisi, J. Geophys. Res. 79, 2849 (1974).

50. E. C. Zipf, W. L. Borst, and T. M. Donahue, J. Geophys. Res. 75, 6371 (1970).

51. R. A. Jones and M. H. Rees, Planet Space Sci. 21, 537 (1973).

52. D. E. Shemanky, E. C. Zipf, and T. M. Donahue, Planet. Space Sci. 19, 1669 (1971).

53. W. E. Sharp and M. H. Rees, J. Geophys. Res. 77, 1810 (1972).

54. A. Chutijian, D. C. Cartwright, and S. Trajmar, Phys. Rev. Lett. 30, 195 (1973).

55. E. S. Oran, P. S. Julienne, and D. F. Strobel, J. Geophys. Res., in press (1975).

56. D. W. Rusch, A. I. Stewart, P. B. Hays, and J. H. Hoffman, J. Geophys. Res., in press (1975).

57. D. F. Strobel, E. S. Oran, P. D. Feldman, and P. S. Julienne, to be published (1975).

58. I. D. Clark and R. P. Wayne, Chem. Phys. Lett. 3, 405 (1969).

59. E. Hyman and P. Julienne, NRL Technical Report #2965 (1975).

60. D. J. Strickland, J. A. Fedder, and T. P. Coffey, NRL Technical Report #2779 (1975).

61. D. F. Strobel, J. Geophys. Res. 76, 2441 (1971).

62. J. H. Kiefer and R. W. Lutz, "The Effect of Oxygen Atoms on the Vibrational Relaxation of Oxygen," 11th Symp. of Combustion, Berkeley, Ca., p. 67 (1966).

63. Reid and Withbroe, Planet. Space Sci. 18 (1970).

64. R. J. McNeal, M. E. Whitson, Jr., and G. R. Cook, J. Geophys. Res. 79, 1527 (1974).

65. R. W. Schunk and P. B. Hays, Planet. Space Sci. 19, 1457 (1971).

66. K. Birkeland, The Norwegian Aurora Polaris Expedition 1902 - 1903, Vol. 1, Sec. 1, H. Aschehong, Christiana, Norway (1908).

67. K. Birkeland, The Norwegian Aurora Polaris Expedition 1902 -1903, Vol. 1, Sec 2, H. Aschehong, Christiana, Norway (1913).

68. P. A. Cloutier, B. R. Sandel, H. R. Anderson, P. M. Pazich, and R. J. Spiger, J. Geophys. Res. 78, 640 (1973).

69. P. A. Cloutier, H. R. Anderson, R. J. Park, R. P. Vondrak, R. J. Spiger, and B. R. Sandel, J. Geophys. Res. 75, 2595 (1970).

70. R. J. Park and P. A. Cloutier, J. Geophys. Res. 76, 7714 (1971).

71. R. T. Casserly, Jr., and P. A. Cloutier, J. Geophys. Res. 80, 2165 (1975).

72. A. J. Zmuda, J. H. Martin, and T. F. Heuring, J. Geophys. Res. 71, 5033 (1966).

73. A. J. Zmuda, F. T. Heuring, and J. H. Martin, J. Geophys. Res. 72, 1115 (1967).

74. A. J. Zmuda, J. C. Armstrong, and F. T. Heuring, J. Geophys. Res. 75, 4757 (1970).

75. J. C. Armstrong and A. J. Zmuda, J. Geophys. Res. 75, 7122 (1970).

76. J. C. Armstrong and A. J. Zmuda, J. Geophys. Res. 79, 4611 (1974).

77. N. M. Vasyliunas, in Particles and Fields in the Magnetosphere, B. M. McCormac (ed.) 60 (1970).

78. R. A. Wolf, Space Sci. Rev. 17, 537 (1975).

79. R. Bostrom, J. Geophys. Res. 69, 4983 (1964).

80. R. A. Wolf, J. Geophys. Res. 75, 4677 (1970).

81. R. K. Jaggi and R. A. Wolf, J. Geophys. Res. 78, 2852 (1973).

82. N. Iwasaki and A. Nishida, Rept. Ionosph. Space Res. Japan 21, 17 (1967).

83. E. T. Karlson, Cosm. Electrodyn. 1, 474 (1971).

84. F. V. Coroniti and C. F. Kennel, J. Geophys. Res. 77, 2835 (1972).

85. D. W. Swift, J. Geophys. Res. 70, 3061 (1965).

86. J. M. Kindel and C. F. Kennel, J. Geophys. Res. 76, 3055 (1971).

87. P. J. Palmadesso, T. P. Coffey, S. L. Ossakow, and K. Papadopoulos, Geophys. Res. Lett. 1, 105 (1974).

88. K. Papadopoulos and T. P. Coffey, J. Geophys. Res. 79, 1558 (1974).

89. K. Papadopoulos and T. P. Coffey, J. Geophys. Res. 79, 674 (1974).

90. D. L. Mathews, M. Pongratz and K. Papadopoulos, to be published in J. Geophys. Res. (1975).

91. L. P. Block, Cosm. Electrodyn. 3, 349 (1972).

92. R. Bostrom,in Magnetospheric Physics, B. M. McCormac (ed.), D. Reidel, Dordrecht-Holland, 45 (1974).

93. J. R. Kan, J. Geophys. Res. 80, 2089 (1975).

94. D. W. Swift, J. Geophys. Res. 80, 2096 (1975).

95. G. Rostoker and R. Boström, Royal Institute of Technology Stockholm, TRITA-EPP-74-25 (1974).

96. A. J. Dessler, J. Geophys. Res. 76, 3174 (1971).

97. G. J. Romick and A. E. Belon, Planet. Space Sci. 15, 1695 (1967).

98. P. M. Banks and G. Kockarts, Aeronomy, Academic Press, New York (1973).

99. L. Spitzer, Jr., Physics of Fully Ionized Gases, John Wiley and Sons, New York (1962).

100. N. C. Maynard, A. Bahnsen, P. Christophersen, A. Egeland, and R. Lundin, J. Geophys. Res. 78, 3976 (1973).

101. N. C. Maynard, J. Geophys. Res. 79, 4620 (1974).

102. J. D. Craven and L. A. Frank, Proc. R. Soc. Lond., A, 343, 167 (1975).

103. T. A. Potemra, Paper presented at Topical Conference on Quantitative Magnetospheric Models, LaJolla, California (1975).

104. H. R. Anderson and P. A. Cloutier, J. Geophys. Res. 80, 2146 (1975).

Preceding Page BLANK - NOT FILMED

DEPARTMENT OF DEFENSE

DIRECTOR
COMMAND CONTROL TECHNICAL CENTER
PENTAGON RM BE 685
WASHINGTON, D.C. 20301
01CY ATTN C-650 G. C. JONES
01CY ATTN C-650 W. HEIDIG
01CY ATTN C-312 R. MASON

DIRECTOR
DEFENSE ADVANCED RSCH PROJ AGENCY
ARCHITECT BUILDING
1400 WILSON BLVD.
ARLINGTON, VA. 22209
01CY ATTN NUCLEAR MONITORING RESEARCH
01CY ATTN STRATEGIC TECH OFFICE

DEFENSE COMMUNICATION ENGINEER CENTER
1860 WIE AVENUE
RESTON, 22090
0 TTN CODE R820 R. L. CRAWFORD
ATTN CODE R410 JAMES W. MCLEAN

DIRECTOR
DEFENSE COMMUNICATIONS AGENCY
WASHINGTON, D.C. 20305
(ADR CNWDI: ATTN CODE 240 FOR)
01CY ATTN CODE 480
01CY ATTN CODE 810 R. W. ROSTRON
01CY ATTN CODE 101B MAJ R. ROOD
01CY ATTN MAUREY RAFFENSPERGER

DEFENSE DOCUMENTATION CENTER
CAMERON STATION
ALEXANDRIA, VA. 22314
(12 COPIES IF OPEN PUBLICATION, OTHERWISE 2 COPIES)
12CY ATTN TC

DIRECTOR
DEFENSE INTELLIGENCE AGENCY
WASHINGTON, D.C. 20301
01CY ATTN DT-1B
01CY ATTN W. WITTIG DC-7D

DIRECTOR
DEFENSE NUCLEAR AGENCY
WASHINGTON, D.C. 20305
01CY ATTN STSI ARCHIVES
01CY ATTN STVL
03CY ATTN STTL TECH LIBRARY
01CY ATTN DDST
03CY ATTN RAAE

DIR OF DEFENSE RSCH & ENGINEERING
DEPARTMENT OF DEFENSE
WASHINGTON, D.C. 20301
01CY ATTN S&SS (OS)

COMMANDER
FIELD COMMAND
DEFENSE NUCLEAR AGENCY
KIRTLAND AFB, NM 87115
01CY ATTN FCPR

DIRECTOR
INTERSERVICE NUCLEAR WEAPONS SCHOOL
KIRTLAND AFB, NM 87115
01CY ATTN DOCUMENT CONTROL

DIRECTOR
JOINT STRAT TGT PLANNING STAFF JCS
OFFUTT AFB
OMAHA, NB 68113
01CY ATTN JLTW-2
01CY ATTN JPST CAPT G. D. GOETZ

CHIEF
LIVERMORE DIVISION FLD COMMAND DNA
LAWRENCE LIVERMORE LABORATORY
P. O. BOX 808
LIVERMORE, CA 94550
01CY ATTN FCPRL

DIRECTOR
NATIONAL SECURITY AGENCY
FT. GEORGE G. MEADE, MD 20755
01CY ATTN JOHN SKILLMAN R52
01CY ATTN FRANK LEONARD
01CY ATTN W14 PAT CLARK

OJCS/J-3
THE PENTAGON
WASHINGTON, D.C. 20301
(OPERATIONS)
01CY ATTN WWMCCS EVAL OFC MR. TOMA

ASD (C31) (SYSTEMS)
3D224, THE PENTAGON
WASHINGTON, D.C. 20301
01CY ATTN DR. M. EPSTEIN
01CY DR. J. BABCOCK

WWMCCS SYSTEM ENGINEERING ORG
WASHINGTON, D.C. 20305
01CY ATTN R. L. CRAWFORD

COMMANDER/DIRECTOR
ATMOSPHERIC SCIENCES LABORATORY
U.S. ARMY ELECTRONICS COMMAND
WHITE SANDS MISSILE RANGE, NM 88002
01CY ATTN DRSEL-BL-SY-S F. E. NILES

DIRECTOR
BMD ADVANCED TECH CTR
HUNTSVILLE OFFICE
P. O. BOX 1500
HUNTSVILLE, AL 35807
01CY ATTN ATC-T MELVIN T. CAPPS
01CY ATTN ATC-O W. DAVIES
01CY ATTN ATC-R DON RUSS

PROGRAM MANAGER
BMD PROGRAM OFFICE
5001 EISENHOWER AVENUE
ALEXANDRIA, VA 22333
01CY ATTN DACS-BMT JOHN SHEA

CHIEF C-E SERVICES DIVISION
U.S. ARMY COMMUNICATIONS CMD
PENTAGON RM 1B269
WASHINGTON, D.C. 20310
01CY ATTN CC-OPS-CE

COMMANDER
HARRY DIAMOND LABORATORIES
2800 POWDER MILL ROAD
ADELPHI, MD 20783
(CNWDI-INNER ENVELOPE: ATTN: DRXDO-RBH)
01CY ATTN MILDRED H. WEINER DRXDO-TI
01CY ATTN DRXDO-RB ROBERT WILLIAMS
01CY ATTN DRXDO-NP FRANCIS N. WIMENITZ
01CY ATTN DRXDO-NP CYRUS MOAZED

DIRECTOR
TRASANA
WHITE SANDS MISSILE RANGE, NM 88002
01CY ATTN ATAA-SA
01CY ATTN TCC/F. PAYAN JR
01CY ATTN ATAA-TAC LTC JOHN HESSE

COMMANDER
U.S. ARMY COMM-ELEC ENGRG INSTAL AGY
FT. HUACHUCA, AZ 85613
01CY ATTN EED-PED GEORGE LANE

COMMANDER
U.S. ARMY ELECTRONICS COMMAND
FORT MONMOUTH, NJ 07703
01CY ATTN DRSEL-NL-RD H. S. BENNET
01CY ATTN DRSEL-PL-ENV HANS A. BOMKE

COMMANDER
U.S. ARMY FOREIGN SCIENCE & TECH CTR
220 7TH STREET, NE
CHARLOTTESVILLE, VA 22901
01CY ATTN P. A. CROWLEY
01CY ATTN R. JONES

COMMANDER
U.S. ARMY MATERIEL DEV & READINESS CMD
5001 EISENHOWER AVENUE
ALEXANDRIA, VA 22333
01CY ATTN DRCLDC J. A. BENDER

COMMANDER
U.S. ARMY NUCLEAR AGENCY
FORT BLISS, TX 79916
01CY ATTN MONA-WE J. BERBERET

DIRECTOR
U.S. ARMY BALLISTIC RESEARCH LABS
ABERDEEN PROVING GROUND, MD 21005
01CY ATTN LAWRENCE J. PUCKETT

COMMANDER
U.S. ARMY SATCOM AGENCY
FT. MONMOUTH, NJ 07703
01CY ATTN DOCUMENT CONTROL

COMMANDER
U.S. ARMY MISSILE INTELLIGENCE AGENCY
REDSTONE ARSENAL, AL 35809
01CY ATTN JIM GAMBLE

CHIEF OF NAVAL OPERATIONS
NAVY DEPARTMENT
WASHINGTON, D.C. 20350
01CY ATTN OP 943 LCDR HUFF
01CY ATTN ALEXANDER BRANDT
01CY ATTN RONALD E. PITKIN

CHIEF OF NAVAL RESEARCH
NAVY DEPARTMENT
ARLINGTON, VA 22217
01CY ATTN CODE 418
01CY ATTN CODE 461

COMMANDER
NAVAL ELECTRONIC SYSTEMS COMMAND
NAVAL ELECTRONIC SYSTEMS CMD HQS
WASHINGTON, D.C. 20360
01CY ATTN NAVALEX 034 T BARRY HUGHES
01CY ATTN PME 117-T SATELLITE COMM PROJECT OFF
01CY ATTN PME 117

COMMANDING OFFICER
NAVAL INTELLIGENCE SUPPORT CTR
4301 SUITLAND ROAD, BLDG. 5
WASHINGTON, D.C. 20390
01CY ATTN MR. DUBBIN STIC 12

COMMANDER
NAVAL OCEAN SYSTEMS CENTER
SAN DIEGO, CA 92152
01CY ATTN WILLIAM F. MOLER
01CY ATTN CODE 0230 C. BAGGETT
03CY ATTN CODE 2200
01CY ATTN R. EASTMAN

DIRECTOR
NAVAL RESEARCH LABORATORY
WASHINGTON, D.C. 20375
01CY ATTN CODE 7700 TIMOTHY P. COFFEY
01CY ATTN CODE 5460 ELECTROMAG PROP BR
01CY ATTN CODE 5430
03CY ATTN CODE 7701 JACK D. BROWN
01CY ATTN HDQ COMM DIR BRUCE WALD (CODE 5400)
01CY ATTN CODE 5465 PROP APPLICATIONS
01CY ATTN CODE 5461 TRANS IONO PROP
01CY ATTN CODE 7750

COMMANDER
NAVAL SPACE SURVEILLANCE SYSTEM
DAHLGREN, VA 22448
01CY ATTN CAPT J. H. BURTON

COMMANDER
NAVAL SURFACE WEAPONS CENTER
WHITE OAK, SILVER SPRING, MD 20910
01CY ATTN CODE WA501 NAVY NUC PRGMS OFF

DIRECTOR
STRATEGIC SYSTEMS PROJECT OFFICE
NAVY DEPARTMENT
WASHINGTON, D.C. 20376
01CY ATTN NSP-2141
01CY ATTN NSSP-2722 FRED WIMBERLY

NAVAL SPACE SYSTEM ACTIVITY
P. O. BOX 92960
WORLDWAY POSTAL CENTER
LOS ANGELES, CALIF. 90009
01CY ATTN A. B. HAZZARD

COMMANDER
ADC/DC
ENT AFB, CO 80912
01CY ATTN DC MR. LONG

COMMANDER
ADCOM/XPD
ENT AFB, CO 80912
01CY ATTN XPQDQ

AF GEOPHYSICS LABORATORY, AFSC
HANSCOM AFB, MA 01731
01CY ATTN OPR HAROLD GARDNER
01CY ATTN OPR JAMES C. ULWICK
01CY ATTN LKB KENNETH S. W. CHAMPION
01CY ATTN OPR ALVA T. STAIR
01CY ATTN SUOL RSCH LIB
01CY ATTN PHP JULES AARONS
01CY ATTN PHD JURGEN BUCHAU
01CY ATTN PHD JOHN P. MULLEN

AF WEAPONS LABORATORY, AFSC
KIRTLAND AFB, NM 87117
01CY ATTN SUL
01CY ATTN CA ARTHUR H. GUENTHER
01CY ATTN DYC CAPT L. WITTWER
01CY ATTN SAS JOHN M. KAMM
01CY ATTN DYC CAPT MARK A. FRY

AFTAC
PATRICK AFB, FL 32925
01CY ATTN TF/MAJ WILEY
01CY ATTN TN

AIR FORCE AVIONICS LABORATORY, AFSC
WRIGHT-PATTERSON AFB, OH 45433
01CY ATTN AAD WADE HUNT
01CY ATTN AFAL AAB H. M. HARTMAN
01CY ATTN AAD ALLEN JOHNSON

HEADQUARTERS
ELECTRONIC SYSTEMS DIVISION/XR
HANSCOM AFB, MA 01731
01CY ATTN XRC LTC J. MORIN
01CY ATTN XRE LT MICHAELS

HEADQUARTERS
ELECTRONIC SYSTEMS DIVISION/YS
HANSCOM AFB, MA 01731
01CY ATTN YSEV

COMMANDER
FOREIGN TECHNOLOGY DIVISION, AFSC
WRIGHT-PATTERSON AFB, OH 45433
01CY ATTN NICD LIBRARY
01CY ATTN ETD B. L. BALLARD

HQ USAF/RD
WASHINGTON, D.C. 20330
01CY ATTN RDQ

COMMANDER
ROME AIR DEVELOPMENT CENTER, AFSC
GRIFFISS AFB, NY 13440
01CY ATTN EMTLD DOC LIBRARY
01CY ATTN OCSE V. COYNE

SAMSO/SZ
POST OFFICE BOX 92960
WORLDWAY POSTAL CENTER
LOS ANGELES, CA 90009
(SPACE DEFENSE SYSTEMS)
01CY ATTN SZJ MAJOR LAWRENCE DOAN

COMMANDER IN CHIEF
STRATEGIC AIR COMMAND
OFFUTT AFB, NB 68113
01CY ATTN XPFS MAJ BRIAN G. STEPHAN
01CY ATTN ADWATE CAPT BRUCE BAUER
01CY ATTN NRT

HEADQUARTERS
ELECTRONIC SYSTEMS DIVISION (AFSC)
HANSCOM AFB, MA 01731
01CY ATTN JIM DEAS

SAMSO/YA
P. O. BOX 92960
WORLDWAY POSTAL CENTER
LOS ANGELES, CA 90009
01CY ATTN YAT CAPT L. BLACKWELDER

SAMSO/SK
P. O. BOX 92960
WORLDWAY POSTAL CENTER
LOS ANGELES, CA 90009
01CY ATTN SKA LT MARIA A. CLAVIN

SAMSO/MN
NORTON AFB, CA 92419
(MINUTEMAN)
01CY ATTN MNNL LTC KENNEDY

COMMANDER
ROME AIR DEVELOPMENT CENTER, AFSC
HANSCOM AFB, MA 01733
01CY ATTN ETEI A. LORENTZEN

EG&G, INC.
LOS ALAMOS DIVISION
P. O. BOX 809
LOS ALAMOS, NM 85544
01CY ATTN JAMES R. BREEDLOVE

UNIVERSITY OF CALIFORNIA
LAWRENCE LIVERMORE LABORATORY
P. O. BOX 808
LIVERMORE, CA 94550
01CY ATTN TECH INFO DEPT L-3
01CY ATTN RONALD L. OTT L-531
01CY ATTN DONALD R. DUNN L-156
01CY ATTN RASPH S. HAGER L-31

LOS ALAMOS SCIENTIFIC LABORATORY
P. O. BOX 1663
LOS ALAMOS, NM 87545
01CY ATTN DOC CON FOR ERIC LINDMAN
01CY ATTN DOC CON FOR R. F. TASCHEK
01CY ATTN DOC CON FOR ERIC JONES
01CY ATTN DOC CON FOR JOHN S. MALIK
01CY ATTN DOC CON FOR MARTIN TIERNEY J-10
01CY ATTN DOC CON FOR JOHN ZINN

SANDIA LABORATORIES
P. O. BOX 5800
ALBUQUERQUE, NM 87115
01CY ATTN DOC CON FOR J. P. MARTIN ORG 1732
01CY ATTN DOC CON FOR W. D. BROWN ORG 1353
01CY ATTN DOC CON FOR A. DEAN THORNBROUGH ORG 1245
01CY ATTN DOC CON FOR T. WRIGHT
01CY ATTN DOC CON FOR D. A. DAHLGREN ORG 1722

OTHER GOVERNMENT

DEPARTMENT OF COMMERCE
OFFICE OF TELECOMMUNICATIONS
INSTITUTE FOR TELECOM SCIENCE
BOULDER, CO 80302
01CY ATTN WILLIAM F. UTLAUT
01CY ATTN G. REED

NATIONAL OCEANIC & ATMOSPHERIC ADMIN
ENVIRONMENTAL RESEARCH LABORATORIES
DEPARTMENT OF COMMERCE
BOULDER, CO 80302
01CY ATTN JOSEPH H. POPE
01CY ATTN RICHARD GRUBB
01CY ATTN C. L. RUFFNACH

NASA
GODDARD SPACE FLIGHT CENTER
GREENBELT, MD 20771
01CY ATTN ATS-6 OFC P. CORRIGAN

DEPARTMENT OF DEFENSE CONTRACTORS

AEROSPACE CORPORATION
P. O. BOX 92957
LOS ANGELES, CA 90009
01CY ATTN IRVING M. GARFUNKEL
01CY ATTN T. M. SALMI
01CY ATTN V. JOSEPHSON
01CY ATTN S. P. BOWER
01CY ATTN N. D. STOCKWELL
01CY ATTN P. P. OLSEN 120 RM 2224E
01CY ATTN F. E. BOND RM 5003
01CY ATTN J. E. CARTER 120 RM 2209
01CY ATTN F. A. MORSE A6 RM 2407

ANALYTICAL SYSTEMS ENGINEERING CORP
5 OLD CONCORD ROAD
BURLINGTON, MA 01803
01CY ATTN RADIO SCIENCES

BOEING COMPANY, THE
P. O. BOX 3707
SEATTLE, WA 98124
01CY ATTN GLEN KEISTER
01CY ATTN D. MURRAY

CALIFORNIA AT SAN DIEGO, UNIV OF
3175 MIRAMAR ROAD
LA JOLLA, CA 92037
01CY ATTN HENRY G. BOOKER

BROWN ENGINEERING COMPANY, INC.
CUMMINGS RESEARCH PARK
HUNTSVILLE, AL 35807
01CY ATTN ROMEO A. DELIBERIS

CHARLES STARK DRAPER LABORATORY, INC.
555 TECHNOLOGY SQUARE
CAMBRIDGE, MA 02139
01CY ATTN D. B. COX
01CY ATTN J. P. GILMORE MS 63

COMPUTER SCIENCES CORPORATION
P. O. BOX 530
6565 ARLINGTON BLVD
FALLS CHURCH, VA 22046
01CY ATTN H. BLANK
01CY ATTN JOHN SPOOR

COMSAT LABORATORIES
LINTHICUM ROAD
CLARKSBURG, MD 20734
01CY ATTN R. R. TAUR

CORNELL UNIVERSITY
DEPARTMENT OF ELECTRICAL ENGINEERING
ITHACA, NY 14850
01CY ATTN D. T. FARLEY JR

ESL INC.
495 JAVA DRIVE
SUNNYVALE, CA 94086
01CY ATTN R. K. STEVENS
01CY ATTN J. ROBERTS
01CY ATTN JAMES MARSHALL
01CY ATTN V. L. MOWER
01CY ATTN C. W. PRETTIE

FORD AEROSPACE & COMMUNICATIONS CORP
3939 FABIAN WAY
PALO ALTO, CA 94303
01CY ATTN J. T. MATTINGLEY MS X22

GENERAL ELECTRIC COMPANY
SPACE DIVISION
VALLEY FORGE SPACE CENTER
GODDARD BLVD KING OF PRUSSIA
P. O. BOX 8555
PHILADELPHIA, PA 19101
01CY ATTN M. H. BORTNER SPACE SCI LAB

GENERAL ELECTRIC COMPANY
TEMPO-CENTER FOR ADVANCED STUDIES
815 STATE STREET (P.O. DRAWER QQ)
SANTA BARBARA, CA 93102
01CY ATTN DASIAC
01CY ATTN DON CHANDLER
01CY ATTN TOM BARRETT
01CY ATTN TIM STEPHENS
01CY ATTN WARREN S. KNAPP
01CY ATTN WILLIAM MCNAMERA
01CY ATTN B. GAMBILL
01CY ATTN MACK STANTON

GENERAL RESEARCH CORPORATION
P. O. BOX 3587
SANTA BARBARA, CA 93105
01CY ATTN JOHN ISE JR
01CY ATTN JOEL GARBARINO

GEOPHYSICAL INSTITUTE
UNIVERSITY OF ALASKA
FAIRBANKS, AK 99701
(ALL CLASS ATTN: SECURITY OFFICER)
01CY ATTN T. N. DAVIS (UNCL ONLY)
01CY ATTN NEAL BROWN (UNCL ONLY)
01CY ATTN TECHNICAL LIBRARY

GTE SYLVANIA, INC.
ELECTRONICS SYSTEMS GRP-EASTERN DIV
77 A STREET
NEEDHAM, MA 02194
01CY ATTN MARSHAL CROSS

INSTITUTE FOR DEFENSE ANALYSES
400 ARMY-NAVY DRIVE
ARLINGTON, VA 22202
01CY ATTN J. M. AEIN
01CY ATTN ERNEST BAUER
01CY ATTN HANS WOLFHARD
01CY ATTN JOEL BENGSTEN

HARRIS CORP, E.S.D.
P. O. BOX 37
MELBOURNE, FL 32901
01CY ATTN ADV PROG DEPT DR. CARL DAVIS

HSS, INC.
2 ALFRED CIRCLE
BEDFORD, MA 01730
01CY ATTN DONALD HANSEN

INTL TEL & TELEGRAPH CORPORATION
500 WASHINGTON AVENUE
NUTLEY, NJ 07110
01CY ATTN TECHNICAL LIBRARY

JAYCOR
1401 CAMINO DEL MAR
DEL MAR, CA 92014
01CY ATTN S. R. GOLDMAN

JOHNS HOPKINS UNIVERSITY
APPLIED PHYSICS LABORATORY
JOHNS HOPKINS ROAD
LAUREL, MD 20810
01CY ATTN DOCUMENT LIBRARIAN
01CY ATTN THOMAS POTEMRA
01CY ATTN JOHN DASSOULAS

LOCKHEED MISSILES & SPACE CO INC
P. O. BOX 504
SUNNYVALE, CA 94088
01CY ATTN DEPT 60-12
01CY ATTN D. R. CHURCHILL

LOCKHEED MISSILES AND SPACE CO INC
3251 HANOVER STREET
PALO ALTO, CA 94304
01CY ATTN MARTIN WALT DEPT 52-10
01CY ATTN RICHARD G. JOHNSON DEPT 52-12
01CY ATTN BILLY M. MCCORMAC DEPT 52-54

KAMAN SCIENCES CORP
P. O. BOX 7463
COLORADO SPRINGS, CO 80933
01CY ATTN B. J. BITTNER

LINKABIT CORP
10453 ROSELLE
SAN DIEGO, CA 92121
01CY ATTN IRWIN JACOBS

M.I.T. LINCOLN LABORATORY
P. O. BOX 73
LEXINGTON, MA 02173
01CY ATTN LIB A-082 FOR DAVID M. TOWLE
01CY ATTN MR. WALDEN X113
01CY ATTN JAMES H. PANNELL L-246
01CY ATTN D. CLARK

MCDONNELL DOUGLAS CORPORATION
5301 BOLSA AVENUE
HUNTINGTON BEACH, CA 92647
01CY ATTN N. HARRIS
01CY ATTN J. MOULE
01CY ATTN GEORGE MROZ
01CY ATTN BILL OLSON

MISSION RESEARCH CORPORATION
735 STATE STREET
SANTA BARBARA, CA 93101
01CY ATTN P. FISCHER
01CY ATTN W. F. CREVIER
01CY ATTN STEVEN L. GUTSCHE
01CY ATTN D. SAPPENFIELD
01CY ATTN R. BOGUSCH
01CY ATTN R. HENDRICK
01CY ATTN RALPH KILB
01CY ATTN DAVE SOWLE
01CY ATTN F. FAJEN
01CY ATTN M. SCHEIBE
01CY ATTN CONRAD L. LONGMIRE
01CY ATTN WARREN A. SCHLUETER

MITRE CORPORATION, THE
P. O. BOX 208
BEDFORD, MA 01730
01CY ATTN J. C. KEENAN
01CY ATTN G. HARDING
01CY ATTN CHIEF SCIENTIST W. SEN
01CY ATTN S. A MORIN
01CY ATTN C. E. CALLAHAN

PACIFIC-SIERRA RESEARCH CORP
1456 CLOVERFIELD BLVD.
SANTA MONICA, CA 90404
01CY ATTN F. C. FIELD JR

PHOTOMETRICS, INC.
442 MARRETT ROAD
LEXINGTON, MA 02173
01CY ATTN IRVING L. KOFSKY

PHYSICAL DYNAMICS INC.
P. O. BOX 21589
SEATTLE, WA 98111
01CY ATTN E. J. FREMOUW

PHYSICAL DYNAMICS INC.
P. O. BOX 1069
BERKELEY, CA 94701
01CY ATTN A. THOMPSON
01CY ATTN JOSEPH B. WORKMAN

R & D ASSOCIATES
P. O. BOX 9695
MARINA DEL REY, CA 90291
01CY ATTN RICHARD LATTER
01CY ATTN FORREST GILMORE
01CY ATTN BRYAN GABBARD
01CY ATTN WILLIAM B. WRIGHT JR
01CY ATTN ROBERT F. LELEVIER
01CY ATTN WILLIAM J. KARZAS

RAND CORPORATION, THE
1700 MAIN STREET
SANTA MONICA, CA 90406
01CY ATTN CULLEN CRAIN
01CY ATTN ED BEDROZIAN

SCIENCE APPLICATIONS, INC.
P. O. BOX 2351
LA JOLLA, CA 92038
01CY ATTN LEWIS M. LINSON
01CY ATTN DANIEL A. HAMLIN
01CY ATTN D. SACHS
01CY ATTN E. A. STRAKER
01CY ATTN CURTIS A. SMITH
01CY ATTN JACK MCDOUGAL

RAYTHEON CO.
528 BOSTON POST ROAD
SUDBURY, MA 01776
01CY ATTN BARBARA ADAMS

SCIENCE APPLICATIONS, INC.
HUNTSVILLE DIVISION
2109 W. CLINTON AVENUE
SUITE 700
HUNTSVILLE, AL 35805
01CY ATTN DALE H. DIVIS

SCIENCE APPLICATIONS, INCORPORATED
8400 WESTPARK DRIVE
MCLEAN, VA 22101
01CY ATTN B. ADAMS

STANFORD RESEARCH INSTITUTE
333 RAVENSWOOD AVENUE
MENLO PARK, CA 94025
01CY ATTN DONALD NEILSON
01CY ATTN ALAN BURNS
01CY ATTN G. SMITH
01CY ATTN L. L. COBB
01CY ATTN DAVID A. JOHNSON
01CY ATTN WALTER G. CHESNUT
01CY ATTN CHARLES L. RINO
01CY ATTN WALTER JAYE
01CY ATTN M. BARON
01CY ATTN RAY L. LEADABRAND

SYSTEM DEVELOPMENT CORPORATION
4130 LINDEN AVENUE
DAYTON, OH 45432
01CY ATTN F. G. MEYER

TECHNOLOGY INTERNATIONAL CORP
75 WIGGINS AVENUE
BEDFORD, MA 01730
01CY ATTN W. P. BOQUIST

TRW DEFENSE & SPACE SYS GROUP
ONE SPACE PARK
REDONDO BEACH, CA 90278
01CY ATTN R. K. PLEBUCH R1-2078
01CY ATTN ROBERT M. WEBB R1-1150

VISIDYNE, INC.
19 THIRD AVENUE
NORTH WEST INDUSTRIAL PARK
BURLINGTON, MA 01803
01CY ATTN CHARLES HUMPHREY
01CY ATTN J. W. CARPENTER